REPORT DOCUMENTATION PAGE

Form Approved
OMB No. 0704-0188

AGENCY USE ONLY (Leave blank)	2. REPORT DATE	3. REPORT TYPE AND DATES COVERED
		Final Report 15 Mar 90-14 Mar 92

TITLE AND SUBTITLE

Optical probes for laser induced shocks

5. FUNDING NUMBERS

AFOSR-90-0210

AUTHOR(S)

Dr Deutsch

7. PERFORMING ORGANIZATION NAME(S) AND ADDRESS(ES)

Massachusetts General Hospital
Wellman Laboratories of Photomedicine
50 Bloosom Street
Boston, MA 02114

AFOSR

8. PERFORMING ORGANIZATION REPORT NUMBER

9. SPONSORING/MONITORING AGENCY NAME(S) AND ADDRESS(ES)

AFOSR/NE
Bldg 410
Bolling AFB DC 20332-6448

10. SPONSORING/MONITORING AGENCY REPORT NUMBER

2301/A1

11. SUPPLEMENTARY NOTES

distribution is unlimited.

12a. DISTRIBUTION/AVAILABILITY STATEMENT

UNLIMITED

12b. DISTRIBUTION CODE

DTIC
ELECTE
OCT 07 1992

13. ABSTRACT (Maximum 200 words)

The support provided by the grant AFOSR-90-0210 has resulted in the publication of four papers and three conference proceedings. Our research covered three topics. (SEE REPORT FOR PROCEEDINGS).

92-26614

14. SUBJECT TERMS			**15. NUMBER OF PAGES**
			16. PRICE CODE

17. SECURITY CLASSIFICATION OF REPORT	18. SECURITY CLASSIFICATION OF THIS PAGE	19. SECURITY CLASSIFICATION OF ABSTRACT	20. LIMITATION OF ABSTRACT
UNCLASSIFIED	UNCLASSIFIED	UNCLASSIFIED	UL

AD-A256 092

FINAL TECHNICAL REPORT ON AFOSR-90-0210

"Optical Probes for Laser-Induced Shocks"

(Covering the period from 15 March 1990 to 14 March 1992)

A.D. Zweig
T.F. Deutsch (P.I.)

Massachusetts General Hospital
Wellman Laboratories of Photomedicine
50 Blossom Street
Boston, MA 02114

August, 1992

SUMMARY

The support provided by the grant AFOSR-90-0210 has resulted in the publication of four papers and three conference proceedings. Our research covered three topics.

First we studied shock waves generated by dielectric breakdown of nano- and picosecond pulses at 1.06 μm wavelength in water [P-1]. We described a non-invasive optical technique to measure the propagation velocity of shock waves in water and showed that during spherical expansion in water the pressure of a shock wave scales as the inverse of the square of the propagation distance and drops to acoustic values within a few hundred microns.

Second we investigated the pressure transients generated during the ablation of sheet polyimide by nanosecond excimer-laser pulses [P-2, C-1, C-2]. We observed the formation of multi-kbar shock waves. The pressures generated during ablation were shown to result from the violent expansion of the rapidly heated gaseous ablation products. Initially, this work used an optical system to measure shock wave velocities. The use of this system was, however, technically quite demanding. We subsequently investigated the use of x-cut quartz gauges to measure shock pressures. The initial measurements using these gauges showed that their sensitivity was insufficient to measure acoustic pressures at or below ablation threshold.

We then developed a system based on PVDF (polyvinylidene fluoride) thin-film transducers which allowed measurement of the pressure transients generated during excimer laser ablation of polyimide for fluences between 30 J/m^2 and 1 MJ/m^2. Measurements were made for four wavelengths: 193, 248, 308, and 351 nm. Three distinct fluence ranges, within which separate physical mechanisms govern pressure generation, were found. In the low fluence regime, the pressure is believed to be due to subsurface thermal decomposition for the two longer wavelengths and to ablative photo-decompositions at the two shorter wavelengths. At higher fluences the pressures result from thermal expansion of ablation products and, at sufficiently high fluences, from plasma formation. The measurement technique, demonstrated for polyimide, also has potential application to biological materials such as bone, skin, and cornea.

Third, in addition, work initiated prior to the AFOSR grant by ADZ at the University of Berne, Switzerland, was completed [P-3, P-4, C-3, C-4, C-5]. That research was concerned with the ablation of tissue and tissue-like targets by pulsed laser radiation in the infrared. A model that explains the ablation process as a combination of evaporation and ejection of liquefied material was developed.

Publications resulting from this grant are attached and describe the research in detail.

PUBLICATIONS AND ABSTRACTS

Publications:

P-1 A.G. Doukas, A.D. Zweig, J.K. Frisoli, R. Birngruber and T.F. Deutsch. Non-invasive determination of shock wave pressure generated by optical breakdown. *Appl. Phys. B*, **53**: 237-245 (1991)

P-2 A.D. Zweig and T.F. Deutsch. Shock waves generated by confined XeCl excimer-laser ablation of polyimide. *Appl. Phys. B*, **54**: 76-82 (1992)

P-3 A.D. Zweig. A thermo-mechanical model for laser ablation. *J. Appl. Phys.*, **70**: 1684-1691 (1991)

P-4 A.D. Zweig. Infrared tissue ablation: Consequences of liquefaction. In: Laser-tissue interaction II, S.L. Jacques, Editor, *Proc. SPIE*, **1427**: 2-8 (1991)

Conference Contributions and Abstracts:

C-1 A.D. Zweig and T.F. Deutsch. Generation of shock waves in confined excimer-laser ablation of polyimide. In: Materials Research Society Symposium Proceedings (C.I.H. Ashby, J.H. Brannon, S.W. Pang, Eds.), Fall Meeting, Boston, MA, *paper B1.10* (1991)

C-2 A.D. Zweig and T.F. Deutsch. Shock waves generated by XeCl excimer-laser ablation of polyimide in air and water. In: Technical Digest, Conference on Lasers and Electro-Optics 1992, *paper CThL4*, p. 512 (1992)

C-3 A.D. Zweig (invited). Infrared tissue ablation: Consequences of liquefaction. SPIE: Laser-tissue interaction II, Los Angeles, CA (1991)

C-4 A.D. Zweig (invited). IR - Ablation of tissue: On the significance of liquefaction. Engineering Foundation Conference, Palm Coast FL (1991) [Unpublished]

C-5 A.D. Zweig. Influence of liquefaction on laser ablation: Drilling depth and target recoil. In: Laser ablation: Mechanisms and applications (J.C. Miller, R.F. Haglund, Jr., Eds.), Proceedings of a Workshop, Oak Ridge, TN, Springer-Verlag *Lecture Notes in Physics*, **389**: 360-362 (1991)

P - 1

Non-Invasive Determination of Shock Wave Pressure Generated by Optical Breakdown

A. G. Doukas, A. D. Zweig, J. K. Frisoli, R. Birngruber*, and T. F. Deutsch

Wellman Laboratory of Photomedicine, Massachusetts General Hospital, Harvard Medical School, Boston, MA 02114, USA

Abstract. Shock waves generated by a laser-induced plasma were investigated using a pump-and-probe technique. Both 7-ns and 40-ps laser pulses at 1.06 μm were employed to initiate breakdown in water. Two He–Ne laser beams were used as a velocity probe, allowing the accurate measurement of the shock velocity around the plasma. The maximum shock pressure was determined from the measured shock velocities, the jump condition and the equation of state for water. The conservation of the total momentum of the shock front was used to derive expressions for the shock velocity, particle velocity and shock pressure vs. the distance (r) from the center of the plasma. For a shock wave of spherical symmetry, the shock pressure is proportional to $1/r^2$. Our work shows that the expanding plasma initially induces a shock wave; the shock wave dissipates rapidly becoming an acoustic wave within 300–500 μm.

The interaction of laser radiation with matter can lead to the generation of pressure waves. Depending upon the type of interaction, the generated waves can be either acoustic waves, low-pressure waves propagating with the speed of sound or shock waves, high-pressure waves propagating at supersonic speed [1]. The latter appear when the absorption of laser radiation is followed by a rapid phase change of the medium such as evaporation or formation of plasma [2, 3].

Our interest in the study of shock waves stems from an increasing awareness that the pressure waves generated during the medical use of lasers may have important effects on tissue. Laser-induced optical breakdown is currently used in two medical applications: kidney stone fragmentation in urology [4] and photodisruption in ophthalmology [5]. In the former application the desired fragmentation of the stone is most likely caused by shock waves. In photodisruption the desired effect is probably caused by the plasma itself; the ancillary shock waves, however, have the potential of causing damage to cells and subcellular structures [6, 7].

The high peak intensity of short duration laser pulses inside a transparent medium leads to optical breakdown.

In the picosecond to nanosecond time regime, the breakdown is initiated via a multiphoton avalanche mechanism [8]. The process begins at the focus of a laser beam, where the laser irradiance is the highest. In water, optical breakdown is followed by the formation of plasma. The high absorbance of the plasma facilitates the deposition of laser energy in the focal zone even in transparent media. Once generated, the hot plasma expands adiabatically with supersonic velocity [9, 10], creating a high pressure front. As the gases in the cavity cool, the expansion velocity of the plasma rapidly decreases and the high pressure front (shock wave) separates from the cavity or bubble. The expansion of the bubble continues until all the initial kinetic energy is transformed into the potential energy of the cavitation. Subsequently, the bubble implodes adiabatically under the external pressure of the liquid. The temperature and pressure inside the bubble rise again leading to a second explosion and the formation of a second shock wave [11].

A primary characteristic of a shock wave is the fast rise time of the pressure wave, which for all practical purposes amounts to a discontinuity in pressure, density, particle velocity and internal energy [12]. In water, the rise time of a shock wave is of the order of a picosecond [13], corresponding to a shock front thickness of a few nanometers. The large pressure gradient and the high translational velocity of the molecules within the shock

* Present address: H. Wacker Labor für Medizinische Laseranwendung, Augenklinik der Universität München. Mathildenstrasse 8, W-8000 München 2, Fed. Rep. Germany

front account for the unique interactions of the shock waves with matter [14, 15].

Since the first measurements of Bell and Landt [3], a number of different techniques have been developed for the study of shock waves. Pressure measurements using transducers [16] have been augmented by optical methods such as Schlieren photography [17], fast photography [18] and optical pump-and-probe techniques [19–21]. The advantage of the optical techniques is that they are non-invasive. In addition, the spatial resolution is potentially high, of the order of micrometers, and the time resolution is only limited by the bandwidth of the detector, currently available in the hundreds of GHz range, corresponding to a time resolution of a few picoseconds.

In previous pump-and-probe experiments [10, 20] the initial shock velocity was calculated from the simultaneous measurement of the radial distance traveled by the shock wave and the time of arrival. We have employed two probe beams, separated by a few tens of micrometers, to measure the shock velocity [22]. This experimental arrangement is insensitive to the temporal and spatial fluctuations in the launching of the shock wave. From the traversal time of the shock front across the two probe beams and the distance between them we derived the shock velocity. Using this high resolution apparatus we have mapped the shock velocity near the plasma, and used the measured shock velocities together with the jump conditions and the equation of state for water to determine the maximum shock pressures from first principles. We have applied the conservation of total momentum of the shock front to derive an expression for the maximum shock pressure as a function of the distance (r) from the center of the plasma. We have found that the maximum pressure is proportional to $1/r^2$.

An important aspect of shock waves as far as medical applications are concerned, is the range over which they can propagate before they dissipate enough energy to become acoustic waves. In this work, we have determined that the range of plasma-induced shock waves is limited to a few hundred micrometers. In comparison, acoustic waves have a range of several tens of millimeters.

1. Experimental

The experimental apparatus is shown in Fig. 1. A Q-switched (Schwartz Electro-Optics) and a mode-locked (Quantel model 501) Nd : YAG laser were used to produce plasma in the sample. Both lasers operated at 1.06 µm and produced pulses of approximately 7 ns and 40 ps, respectively. The energy of the lasers was monitored with a Scientech (model 365) or a Molectron (model J3-09) energy meter. The pump pulse was focused by a 12-mm focal length aspheric lens. The beam waist in air was estimated using burn paper. It was of the order of 50 µm, yielding an irradiance in the range of 10^{10} to 10^{11} W/cm^2 for the nanosecond and 10^{11} W/cm^2 for the picosecond pulses, respectively. The beam waist in water, however, would be bigger. The sample, distilled and deionized water, was circulated and filtered in order to remove bubbles and any other impurities generated during the breakdown.
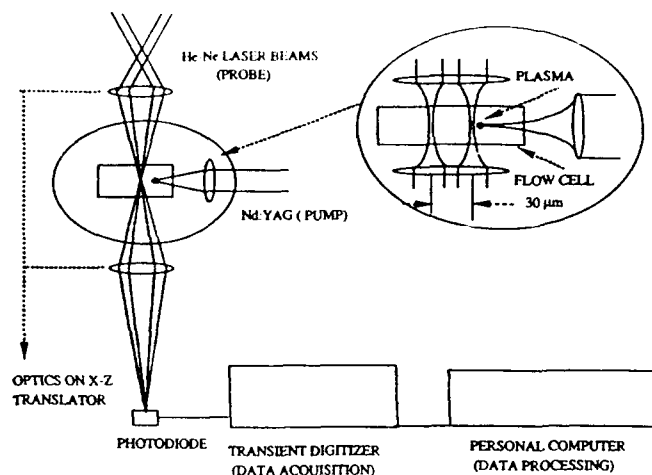

Fig. 1. The experimental apparatus. Two He–Ne laser beams are used to determine the velocity of the shock wave

Two He–Ne laser beams separated by 30–40 µm were used to measure the shock velocity. The system of the directing mirrors, focusing and collecting optics for the probe beams was placed on an $X - Z$ translation stage, X being the axis of the pump beam (axial) and Z the axis perpendicular to it (radial). A dove prism in the path of the two He–Ne beams was used to make the plane of the two beams either horizontal or vertical, depending on whether the measurements were carried out along the axial or radial direction. The two He–Ne beams exiting from the cell were recombined and directed onto a single Si photodiode (EG & G model FND 100). The active area of the detector was 5 mm^2 and the rise time < 1 ns. The signal was recorded by a transient digitizer (Tektronix 7912 AD, 750 MHz bandwidth) and transferred to an IBM-AT PC computer for processing.

The shock wave induces a discontinuity in the index of refraction of the medium due to the density increase in the shock front. This results in the deflection of the He–Ne laser beam, and the intensity of the light transmitted to the detector is decreased. As the shock wave propagates through the two probe beams, it generates two separate pulses. On the other hand, the passage of the cavitation bubble through the probe beams produces a stepped signal, resulting from the interruption of one and then both beams. The shock velocity was determined from the time interval between the two pulses and the separation distance of the two probe beams. In addition, the time interval between the two steps was used to determine the expansion velocity of the plasma or the cavitation bubble.

Figure 2 shows a series of photodiode signals taken at different distances from the center of the plasma: (a) at the center of the plasma where both beams were blocked, (b) and (c) where the shock wave is initially launched by the expanding plasma, (d) in the proximity of the breakdown region after the shock wave had separated from the bubble, while (e) shows the photodiode signal in the far field. The waveforms presented in Fig. 2b and d correspond to the stages of the plasma evolution depicted
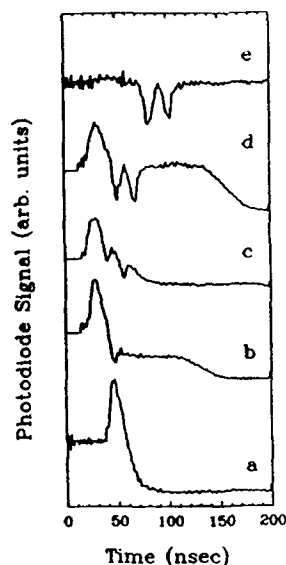
Time (nsec)

Fig. 2. The photodiode signal taken at different positions: (a) the center of the plasma, (b) the edge of t'e plasma, (c) the initial separation of the shock wave from the plasma, (d) in the near field and (e) in the far field. Rapid events, like the deflection of the beams by the spatially-thin shock wave front, result in two separate pulses. Long term events, like the passage of a cavitation bubble, produce a stepped signal, resulting from the interruption of one and then both, beams. The time between the two pulses is related to the shock velocity, while the time interval between the two steps that follows is related to the velocity of the expansion of the cavitation or bubble. The increased signal at the beginning of the trace is caused by the emitted light from the plasma

Fig. 3. A schematic representation of the shock wave generation during optical breakdown: (a) plasma initiation, (b) plasma expansion, (c) separation of the shock wave from the plasma, (d) collapse of the bubble

in Fig. 3b and c. The cavitation bubble can undergo several cycles of nearly adiabatic expansion and contraction. Figure 4 illustrates this for the case when three cavitation bubbles are formed. Note that the second and third bubbles produce half as large a signal as the first, indicating that they have not propagated to the second probe beam.

The shape of the photodiode signal was an almost symmetric pulse of 10 ns (FWHM). The rise time correlated to the traversal time of the shock front through the waist of the probe beam. The decay of the signal, however, could be altered by changing the diameter of the aperture in front of the photodiode. We found that the best time resolution could be obtained by keeping the aperture open. In this case, the diameter of the collecting lens is the effective aperture. Under these conditions, the photodiode signal does not represent the course of the pressure wave in our experimental arrangement. Decay times of shock waves, reported in the literature, vary from 10 to 40 ns [21, 23]. A possible explanation for the short duration of the signal in our experiments is that the deflection of the beam is highest when the incident beam is at grazing angle to the spherical shock front. Therefore, only the leading edge of the shock wave causes a large deflection that can be detected.

The photodiode signal decreases by a factor of three between the near and far fields. The signal intensity depends on the pressure of the shock wave. In this work, we did not try to calculate the shock pressure from the intensity of the signal. The change in the index of re-
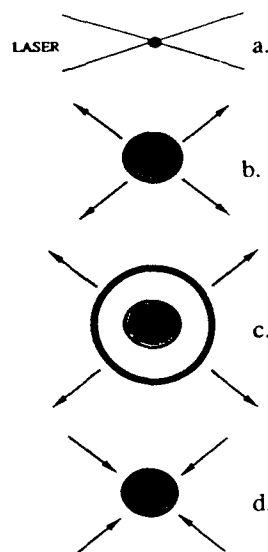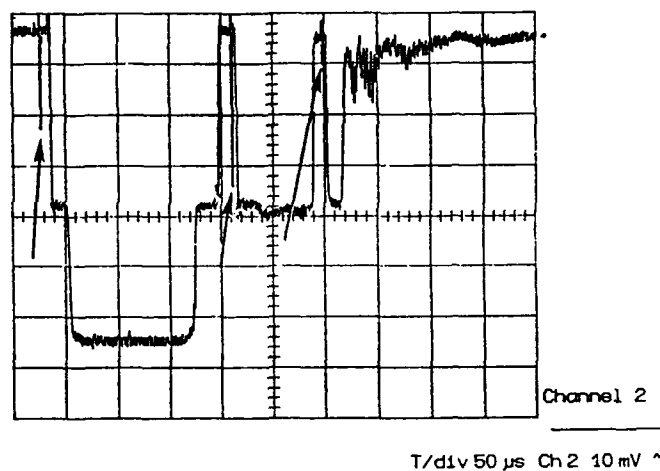

T/div 50 µs   Ch 2   10 mV ~

Fig. 4. Oscilloscope trace of the probe signal caused by a series of three expansions and contractions of a cavity. Each collapse of the bubble is followed by the generation of a shock wave as shown by the arrows. The second and third bubbles produce half as large a signal as the first because they have not propagated to the second probe beam

fraction, caused by the pressure, is proportional to the pressure rise only up to 2 kbar, for higher pressure values it increases less than linearly [19, 24]. These types of measurements, however, require an accurate calibration of the detector, which is not necessary when the measured quantity is the time between the two pulses.

The boundaries of the plasma were determined using the probe beams. The probe beams were translated through the plasma to the position where both beams were blocked. The positions for total blockage of the probe beams in either direction gave the plasma extremes. The mean values of the two positions in the axial and radial directions were taken as the coordinates of

the geometrical center of the plasma. It should be noted that the center of the plasma, as defined, may not coincide with the focal point of the pump beam [25] or the center of curvature of the expanding shock wave. This, however, is more likely to be significant in the axial than in the radial direction. We will return to this point in the discussion.

The pressure-wave velocity was measured radially and axially as far as 1500 μm away from the center of the plasma, on both sides of it. The range was chosen so that there was a sufficient number of measurements in the far field where the pressure wave propagates with sound velocity. In fact, the constancy of the measured velocity in the far field was taken to imply that the sound velocity had been reached. The distance between the two He–Ne probe beams was determined from the traversal time in the far field and the sound velocity, 1.483 km/s in distilled water at 20° C. The distance between the two beams was typically 30–40 μm. Close to the plasma, the shock velocity was measured in steps of 20 μm. In the far field, where changes in the velocity were small, the velocity of the pressure wave was measured at intervals of 50 or 100 μm. There were considerable fluctuations of the shock velocity in the proximity of the plasma, the standard deviation of the measured velocities ranging from 60 m/s to 140 m/s. The velocity fluctuations were attributed to the statistical nature of the shock wave generation and the variation of the pulse energy. The velocity fluctuations decreased gradually with increasing distance from the plasma, correlating with the dissipation of the shock wave and the appearance of the acoustic wave. The standard deviation of the measured velocity in the far field provides a measure of the velocity resolution of the apparatus. The standard deviation of the measured sound velocity ranged between 15 m/s and 20 m/s, corresponding to a resolution of the experimental apparatus of ~ 30–40 m/s or 2–3%.

The plasma duration produced by the nanosecond pulses was of the order of 15 ns. The emission spectrum of the plasma was collected with an optical fiber coupled to 1/4-meter flat-field spectrograph and measured using a gated (30 ns) optical multichannel analyzer (EG & G OMA III). The emission spectrum showed a broad structureless band with the maximum intensity at ~ 370 nm. Using Wien's law ($\lambda_m T$ = 0.29 K · cm), we have calculated a plasma temperature of ~ 8000 K which is of the same order of magnitude as the plasma temperatures reported in the literature [9]. The emission spectrum, however, deviated from that of black-body radiation in the long wavelength region, possibly because the gate was too long to allow temporal resolution of the changing spectral emission and the observed spectrum was the superposition of the spectra emitted during the evolution of the plasma.

The plasma size depended on the energy and duration of the laser pulse. Nanosecond pulses with energy of 2 3 mJ generated plasmas that were spherical or ellipsoidal with a ratio of major (axial) to minor (radial) axes varying from 1:1 to 1.5:1, the minor axis being approximately 80 100 μm. When the energy increased to 11 15 mJ, the ratio of the axes ranged from 2:1 to 2.5:1, and the minor

axis increased to 120 150 μm. The breakdown threshold was 1-2 mJ. For picosecond pulses, 3 mJ, the ratio of the two axes was 3:1, the minor axis being approximately 50 μm. In both cases the plasma dimensions varied from pulse-to-pulse with the axial dimension varying more than the radial.

2. Results

Figure 5 shows the results of a typical measurement of the shock velocity produced by nanosecond laser pulses and measured axially from the center of the plasma. Similar results were obtained in the radial direction. Each experimental point is the average of ten measurements and the error bars are the standard deviations. The measured shock velocity varies from ~ 2.2 km/s at a distance of ~ 120 μm from the center of the plasma to that of the sound velocity at 500 μm away from the center of the plasma. Our measurements in the proximity of the plasma agree with the velocity measured by Fujimoto et al. [20].

The shock wave pressure is related to the shock velocity through Newton's second law across the shock wave discontinuity.

$$P - P_0 = U_s u_p \varrho_0, \tag{1}$$

where P and P_0 are the shock and the hydrostatic pressure, respectively, U_s the shock velocity, u_p the particle velocity and ϱ_0 the density of the water before compression. P_0 is much smaller than the shock pressure and can be neglected. Equation 1 and the equations that describe the conservation of mass and energy across the shock wave discontinuity are known as the jump conditions.

The shock and particle velocities are related through the equation of state. To a first approximation, it can be written as

$$U_s = A + B u_p. \tag{2}$$

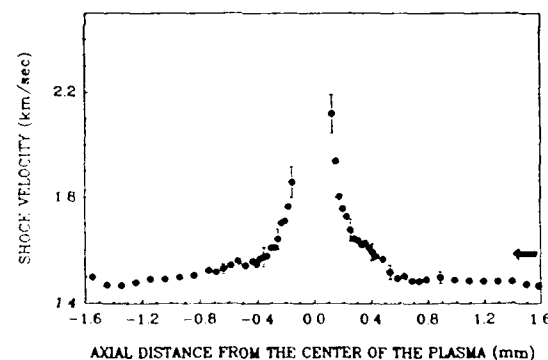AXIAL DISTANCE FROM THE CENTER OF THE PLASMA (mm)

Fig. 5. Shock velocity measured axially vs. distance from the center of the plasma. The shock wave was generated by a 2.6 mJ pulse from a Q-switched Nd : YAG laser. The arrow indicates the direction of the exciting laser pulse. Each experimental point is the average of ten measurements. The large difference in the values of the shock velocity at the proximity of the plasma is to some extent accounted for by the different minimum distances from the center plasma: for example 127 μm at the proximal side, 150 μm at the distal side. The error bars represent the standard deviation.
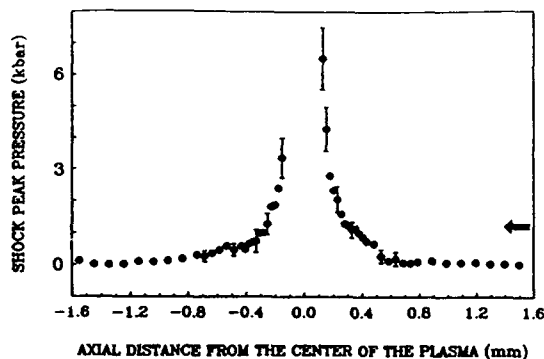
Fig. 6. Shock peak presssure vs. axial distance from the center of the plasma. Each point is the average of ten values of pressure determined separately from the shock velocities shown in Fig. 5. The error bars represent the pressure standard deviation. The arrow indicates the direction of the exciting laser pulse

For water, the values of A and B are 1.48 km/s and 2.07, respectively [26]. U_s and u_p are given in km/s. Note that the value of A is the sound velocity. These values of A and B are valid for up to 20 kbar. A higher order approximation is given in [27]. From Eqs. (1) and (2) the shock pressure is calculated, as shown in Fig. 6. The calculated pressures range from 8 kbar (8×10^8 Pa) at a distance of $\sim 100\,\mu$m from the center of the plasma to a few hundred bar at a distance of 500 μm.

The propagation of the shock wave involves the inelastic collisions of the water molecules within the shock front. For a shock wave that has separated from the expanding bubble, the total momentum of the shock front is conserved. For a spherically symmetric shock wave, the conversation of the total momentum at a distance r from the center of the plasma can be written as:

$$4\pi r^2 U_s \Delta t \varrho u_p = \text{const},\qquad(3)$$

where Δt is the rise time and ϱ the density of the medium in the shock front. The density within the shock front changes from ϱ_0 to that of the compressed state. The density of water, even at 10 kbar, increases by less than 15% [27] and can be considered constant. Δt is the rise time of the shock front and is constant in the range of 0–100 kbar [13]. Substituting u_p from the equation of state of water (2) into (3), we derive

$$U_s(U_s - A) = \frac{C}{r^2},\qquad(4)$$

where C includes the constants B, ϱ and Δt. Equation (4) can be solved for U_s to derive the expression of the shock velocity vs. distance from the center of the plasma

$$U_s(r) = \frac{A}{2} + \sqrt{\frac{A^2}{4} + \frac{C}{r^2}}.\qquad(5)$$

Equation (5) is the mathematical expression used to fit the measured velocities of the shock waves generated by nanosecond and picosecond pulses in both radial and axial directions. The constant C was calculated by a weighted linear regression using the measured values of the velocity vs. distance. For the purpose of fitting (4) can be written as $Y = CX$ where $Y = U_s(U_s - A)$

and $X = 1/r^2$. The value of C is not sensitive to the measured velocities in the far field. In fact, the difference in the value of the constant obtained by using the full range of measurements (± 1500 μm) instead of a reduced range (± 450 μm) is less than 10%. The justification for using a truncated range is that the shock wave range is of the order of 500 μm.

There are two sources of error in the measurement of the shock velocity. First, the calculated shock velocity is a statistical average of many separate measurements, rather than the velocity of a single generated shock wave. Second, the velocity measured is the average velocity between the two probe beams which can be written as:

$$\langle U_s(r) \rangle = (1/L) \int_{r-(L/2)}^{r+(L/2)} U_s(r')dr',\qquad(6)$$

where L is the distance between the two probes and $U_s(r')$ is the shock velocity, given by (5). The integral can be evaluated but the derived expression is complicated and not easily amenable to a standard fitting procedure. In view of the large fluctuations of the measured shock velocities, the use of a deconvolution procedure would not add to the accuracy of the present analysis. In fact, the numerical evaluation of integral 6 over a distance of 40 μm (the distance between the two probes) gave a value that was within the experimental standard deviation of the measured shock velocity.

Substituting (5) into (2) (equation of state), we derive an expression for the particle velocity:

$$u_p(r) = \frac{1}{B} \left(\sqrt{\frac{A^2}{4} + \frac{C}{r^2}} - \frac{A}{2} \right).\qquad(7)$$

We can use (7) to extrapolate the particle velocity at the onset of the shock wave. The shock wave separates from the cavitation when the particle velocity, that is the velocity of the displacement of the matter behind the shock front, exceeds the velocity of the bubble expansion. The

Table 1. Comparison of the bubble expansion velocity and particle velocity at the onset of the shock wave

Energy	Distance	Bubble velocity	Particle velocity	Pressure
[mJ]	[μm]	[km/s]	[km/s]	[kbar]
Nanosecond-generated shock wave				
3.6 (R)	− 60	0.26	0.52	13.1
	+ 60	0.30	0.52	
5.7 (R)	+110	0.49	0.37	8.4
14.7 (R)	−120	0.50	0.57	15.3
	+120	0.49	0.57	
2.6 (A)	−110	0.33	0.32	6.7
	+102	0.38	0.42	9.9
11.3 (A)	−203	0.39	0.23	4.6
	+203	0.38	0.24	6.1
Picosecond-generated shock wave				
3.3 (R)	− 50	0.24	0.48	11.9
	+ 50	0.29	0.48	

R and A stand for radial and axial directions. The particle velocity and pressure were extrapolated from (7) and (8) respectively

expansion of the bubble can be measured. The time interval between the two steps, in Fig. 2b, corresponds to the traversal time of the expanding plasma between the two probe beams. From the traversal time and the distance between the two beams, we calculated the velocity of expansion. Table 1 shows the measured values of an average velocity of the plasma expansion and the calculated particle velocities. In most cases the agreement is very good. The process of separation of the shock wave from the cavitation described here is limited by the temporal resolution of our experimental apparatus. The actual process may be much more complex.

2.1 Radial Shock Velocity

Figures 7 and 8 show the measured radial velocities of the shock waves generated by nanosecond and picosecond pulses, respectively. The lines represent the theoretical fit of (5) to the data of both branches. Equation (5) can also be fitted separately to each of the branches. The difference, however, is within the experimental error. The theoretical curves agree reasonably well with the measured shock velocities, considering the simplicity of the model used. The same expression for the shock veloc-
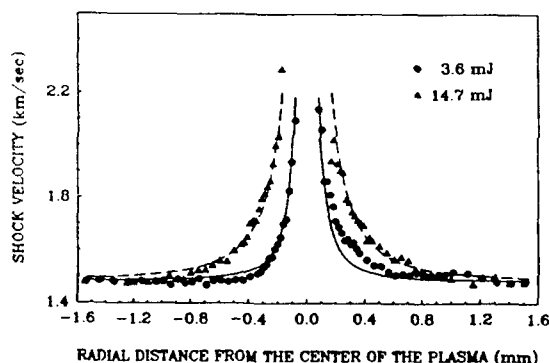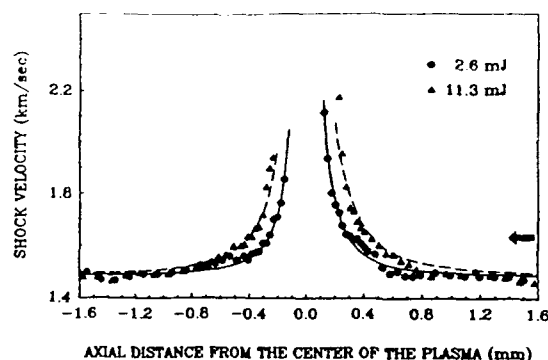
Fig. 9. Shock velocities vs. axial distance. The shock waves were generated by 2.6 or 11.3 mJ pulses from a Q-switched laser. The lines are the theoretical fit as given by (5). Both branches of the theoretical curve begin at the same distance from the center of the plasma. Each branch was fitted separately. The arrow indicates the direction of the exciting laser pulse

ity vs. distance applies to the shock waves generated by picosecond and nanosecond pulses. In this respect the pulse duration, at least in the range 10^{-11}–10^{-8} s, does not affect the scaling of the shock velocity. The constant in the expression, however, does depend on the laser parameters.

2.2 Axial Shock Velocity

Figure 9 shows the axial velocity of the shock waves generated by nanosecond pulses at two energy levels. The positive axis corresponds to the proximal position, the side of the plasma closest to the incoming laser pulse. It appears that the shock velocities at the proximal side are higher than those at the distal side. The difference, however, is still within the standard deviation of the measurements. It is possible that the shock velocity and thus the pressure is higher at the proximal side. This could be explained by the way the plasma expands during the laser pulse; the proximal side practically shielding the distal side [28, 29]. In the theoretical curves presented here, the two branches have been fitted separately.

The difficulty in the analysis of the axial velocities is that the center of the plasma, as we mentioned earlier, cannot be determined unambiguously. Taking a different point along the axial direction as center would affect the value of the constant (C) considerably. It would not, however, affect the calculated pressure. This is because the two-beam method gives an absolute magnitude of the shock velocity.

Picosecond-generated plasma showed no discernible shock waves in the axial direction. Recent experiments by Vogel and co-workers using fast photography showed that the picosecond-generated plasma is not completely homogeneous and that, at the proximal side, it consists of a large number of microplasmas [30]. Figure 10 shows the plasma and the shock wave generated by a 3.6-mJ, 30-ps laser pulse 30 ns after optical breakdown [30]. In the radial direction the shock waves combine to create a measurable effect, while in the axial direction, they are

Fig. 7. Shock velocities vs. radial distance. The shock waves were generated by 3.6 or 14.7 mJ pulses from a Q-switched laser. The lines are the theoretical fit as given by (5). Both branches were fitted simultaneously
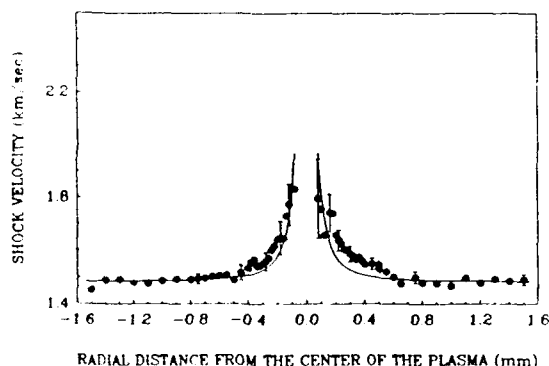
Fig. 8. Shock velocities vs. radial distance. The shock waves were generated by a 3.3-mJ pulse from a mode-locked laser. The line is the theoretical fit as given by (5). Both branches were fitted simultaneously
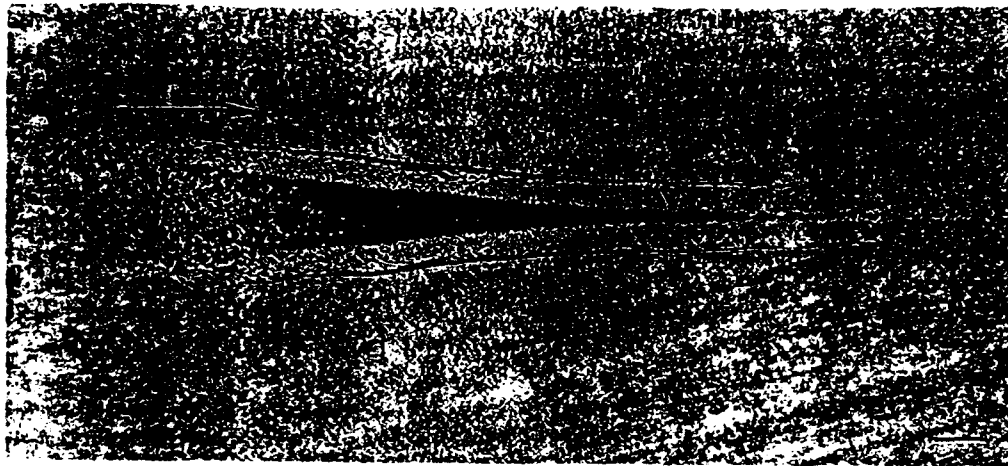
Fig. 10. Picosecond-generated plasma by a 3.6-mJ laser pulse showing a large number of microplasma. The photograph was taken 30 ns after the optical breakdown. Note the appearance of the shock wave in the radial direction only. The arrow indicates the direction of the exciting laser pulse. The bar equals 100 μm. The photograph was taken by Dr. A. Vogel of H. Wacker Laboratory, Munich and is reproduced by permission

reflected on the surface of the neighboring microplasmas and dissipate. The large impedance difference between the liquid and gaseous phases accounts for the efficient reflection and scattering of the shock waves, so that no shock waves appear in the axial direction.

3. Discussion

The shock wave pressure can be calculated from the shock and particle velocities and the jump condition. If (5) and (7) are substituted into (1), we derive an expression for the pressure as a function of the distance from the center of the plasma

$$P = C \frac{\varrho_0}{B} \frac{1}{r^2}. \tag{8}$$

Figures 11 and 12 show the calculated shock wave pressures in the radial and axial directions, respectively. The present work seems to contradict measurements of pressure waves using transducers, which show that the pressure for spherically expanding waves is proportional to $1/r$ [16] rather than to $1/r^2$. It should be noted, however, that the pressure calculated from our velocity measurements relates only to the shock waves. The shock pressure decreases rapidly so that at distances over 500 μm it is practically zero. The far field pressure computed from the shock velocity is not accurate because the velocity of the pressure wave is very close to the velocity of sound and the resolution of our techniqu: is not sufficient to allow for an accurate measurement of the velocity in this range. Consequently, the pressure in the far field is underestimated. Equation (8) is valid only in the near field where the pressure waves generated by the optical breakdown are manifested as shock waves.

The optical measurements, taken together with the transducer measurements, seem to support the concept that the plasma initially generates a shock wave, the pressure of which is proportional to $1/r^2$. The shock wave dissipates rapidly and continuous as an acoustic wave that decays as $1/r$. The difference in the scaling laws for the two types of waves (supersonic vs. sonic) results from the attenuation mechanisms. In the sonic
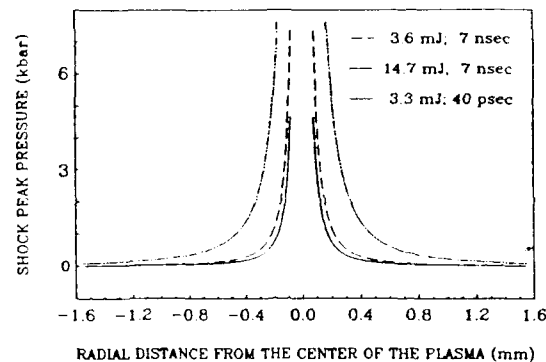
Fig. 11. Shock peak pressure vs. radial distance calculated from (8). The three curves correspond to the three sets of measurements of the shock velocities shown in Figs. 7 and 8
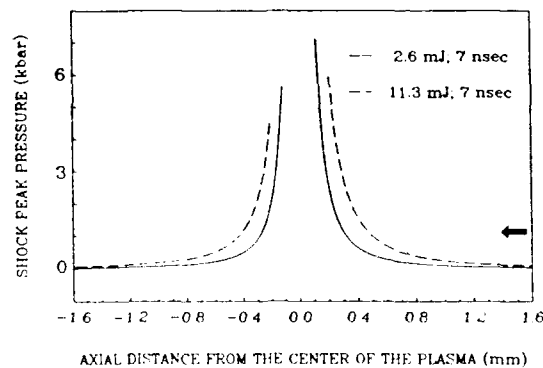
Fig. 12. Shock peak pressure vs. axial distance calculated from (8) The two curves correspond to the two sets of measurements of the shock velocities shown in Fig. 9. The arrow indicates the direction of the exciting laser pulse

region, the energy of the wave is conserved provided that the medium does not absorb the sound. For a spherically expanding wave, the average kinetic energy within a thin layer at a distance r from the center of the plasma can be written as

$$I = 4\pi r^2 I \tag{9}$$

Equation (9) leads to a pressure that is proportional to $1/r$. A shock wave, on the other hand, involves irreversible processes, wherein the kinetic energy within the shock front is converted into heat. In this case, the momentum but not the kinetic energy is conserved. For a spherically expanding shock wave the pressure is proportional to $1/r^2$. The existence of two different mathematical expressions for the pressure implies that the pressure in the near field cannot be deduced from pressure measurements in the far field unless, of course, the proportionality constant in the two expressions is the same.

It can also be instructive to compare our results (8) with two theories developed for underwater explosions [31], namely Kirkwood-Bethe and Penney-Dasgupta. Of the two, Penney-Dasgupta theory provides a simple expression for the maximum pressure which is valid in the proximity of the explosion,

$$P = G(a_0/r)\exp(2a_0/r) \tag{10}$$

where a_0 is the linear dimension of the explosive and G a constant. We can fit (10) to our measurements taking as a_0 the linear dimension of the plasma. The fit is good except in the far field where (10) predicts higher pressures. We know, however, that our determination of the pressure in the far field is not accurate, as it has been discussed in the experimental section. We can approximate (10) with the first two terms of a power series expansion, since a_0/r is less than one in our measurements.

$$P = G(a_0/r) + 2G(a_0/r)^2 + \dots. \tag{11}$$

The first term corresponds to the acoustic wave that remains after the dissipation of the shock wave. The second term becomes dominant in the near field and corresponds to the shock wave. An important implication of the Penney-Dasgupta expression is that it may provide a way to extrapolate the shock pressure in the near field from acoustic pressure measurements in the far field.

Underwater shock wave research has established that the shock pressure scales as the linear dimension of the explosive [31]. The fact that (10) fits our measurements, when a_0 is taken as the linear size of the plasma, indicates that a similar scaling law may operate in the case of plasma-induced shock waves. In fact, some of our measurements in the radial direction are consistent with a similar scaling law. The shock pressures, expressed as a function of normalized distance from the center of the plasma r/a_0, are the same. The difficulty in establishing this scaling law unambiguously in our experiments is related to the fluctuations in both the size of the plasma and the shock velocity. In our measurements the shock velocity is the average velocity of many separate shock waves while a_0 is the smallest linear dimension. What may be needed is the simultaneous measurement of the plasma size and the shock velocity.

4. Conclusions

We have used a two-beam probe to measure the shock velocity around a laser-induced plasma. We have demon-

strated that the technique is accurate enough to measure the shock velocity and hence determine the shock maximum pressure non-invasively. We have used the principle of conservation of total momentum of the shock front to derive expressions for the shock velocity, particle velocity and pressure vs. the distance from the center of the plasma. Our work supports the concept that the expanding plasma initially induces a shock wave which dissipates rapidly into an acoustic wave. In addition, we have found that the range of the shock wave is limited compared to the range of acoustic waves. Thus, tissue damage caused by shock waves should also have a limited range.

References

1. D.A. Hutchins: Ultrasonic generation by pulsed lasers. Physical Acoustics 18, 21–123 (1988)
2. C.E. Bell, B.S. Maccabee: Shock wave generation in air and water by CO_2 TEA laser radiation. Appl. Opt. 13, 605–609 (1974)
3. C.E. Bell, S.A. Landt: Laser-induced high-pressure shock waves in water. Appl. Phys. Lett. 10, 46–48 (1967)
4. S.P. Dretler: Laser lithotripsy: a review of 20 years of research and clinical applications. Lasers Surg. Med. 8, 341–356 (1988)
5. R.F. Steinert, C.A. Puliafito: The Nd:YAG Laser in Ophthalmology: Principles and Clinical Applications of Photodisruption (Saunders, Philadelphia 1985)
6. P. Russo, C. Mies, R. Huryk, W.D.W. Heston, W.R. Fair: Histopathologic and ultrastructural correlates of tumor growth suppression by high energy shock waves. J. Urol. 137, 338–341 (1987)
7. F. Brümmer, J. Brenner, T. Bräunel, D.F. Hüsler: Effects of shock waves on suspended and immobilized L1210 cells. Ultrasound Med. Biol. 15, 229–239 (1989)
8. E.W. Van Stryland, M.J. Soileau, A.L. Smirl, W.E. Williams: Pulse-width and focal-volume dependence of laser-induced breakdown. Phys. Rev. B 23, 2144–2151 (1981)
9. P.A. Barnes, K.E. Rieckhoff: Laser-induced underwater sparks. Appl. Phys. Lett. 13, 282–284 (1968)
10. B. Zysset, J.G. Fujimoto, T.F. Deutsch: Time-resolved measurements of picosecond optical breakdown. Appl. Phys. B 48, 139–147 (1989)
11. R. Hickling, M.S. Plesset: Collapse and rebound of a spherical bubble in water. Phys. Fluids 7, 7–14 (1964)
12. G.E. Duvall, G.R. Fowles: Shock waves, in High Pressure Physics and Chemistry, Vol. 2, ed. by R.S. Bradley (Academic, New York 1963) pp. 209–291
13. P. Harris, H.N. Presles: The shock-induced electrical polarization of water. J. Chem. Phys. 77, 5157–5164 (1982)
14. G.E. Duvall, K.M. Ogilvie, R. Wilson, P.M. Bellamy, P.S. Wei: Optical spectroscopy in a shocked liquid. Nature 296, 846–847 (1982)
15. See for example Shock Waves in Condensed Matter - 1987, Proceedings of the American Physical Society Conference 1987; ed. by S.C. Schmidt, N.C. Holmes (Elsevier, Amsterdam 1988)
16. H. Schoeffmann, H. Schmidt-Kloiber, E. Reichel: Time-resolved investigations of laser-induced shock waves in water by use of

polyvinylidenefluoride hydrophone. J. Appl. Phys. **63**, 46–61 (1988)

17. G.P. Davidson, D.C. Emmony: A Schlieren probe method for the measurement of the refractive index profile of a shock wave in a fluid. J. Phys. E **13**, 92–97 (1980)

18. W. Lauterborn: High speed photography of laser-induced breakdown in liquids. Appl. Phys. Lett. **31**, 27–29 (1972)

19. B. Sullivan, A.C. Tam: Profile of laser-produced acoustic pulse in a liquid. J. Acoust. Soc. Am. **75**, 437–441 (1984)

20. J.G. Fujimoto, W.Z. Lin, E.P. Ippen, C.A. Puliafito, R.F. Steinert: Time-resolved studies of Nd:YAG laser-induced breakdown. Invest. Ophthalmol. Vis. Sci. **26**, 1771–1775 (1985)

21. A. Vogel, W. Lauterborn: Acoustic transient generation by laser-produced cavitation bubbles near solid boundaries. J. Acoust. Soc. Am. **84**, 719 731 (1988)

22. A.G. Doukas, R. Birngruber, T.F. Deutsch: Determination of shock wave pressures generated by laser-induced breakdown in water, in *Laser-Tissue Interactions*, ed. by S.L. Jacques, Proc. SPIE **1202**. 61–70 (1990)

23. K. Hinch, E. Brinkmeyer: Investigation of very short cavitation shock waves by coherent optical methods, in *High Speed Photography*, ed. by M.C. Richardson. Proc. SPIE **97**, 166–171 (1976)

24. K. Vedam, P. Limsuwan: Piezo-optic behaviour of water and carbon tetrachloride under high pressure. Phys. Rev. Lett. **35**, 1014–1016 (1975)

25. A. Vogel, P. Schweiger, A. Frieser, M.N. Asiyo, R. Birngruber: Intraocular Nd:YAG laser surgery: Light-tissue interaction, damage range, and reduction of collateral effects. IEEE J. QE-**26**, 2240–2260 (1990)

26. P. Harris, H N. Presles: Reflectivity of a 5.8 kbar shock front in water. J. Chem. Phys. **74**, 6864–6866 (1981)

27. U.H. Rice, J.M. Walsh: Equation of state of water to 250 kbar. J. Chem. Phys. **26**, 824–830 (1957)

28. F. Docchio, P. Regondi, M.R.C. Capon, J. Mellerio: A study of the temporal and spatial dynamics of plasmas induced in liquids by nanosecond Nd:YAG laser pulses. I. Analysis of the plasma starting times. Appl. Opt. **27**, 3661–3668 (1988)

29. F. Docchio, P. Regondi, M.R.C. Capon, J. Mellerio: A study of temporal and spatial dynamics of plasmas induced in liquids by nanosecond Nd:YAG laser pulses. II. Plasma luminescence and shielding. Appl. Opt. **27**, 3669–3674 (1988)

30. A. Vogel: Private communication

31. R.H. Cole: *Underwater Explosions* (Princeton University Press, Princeton 1948)

p. 2

Shock Waves Generated by Confined XeCl Excimer Laser Ablation of Polyimide

A. D. Zweig and T. F. Deutsch

Wellman Laboratories of Photomedicine, Massachusetts General Hospital, Boston, MA 02114, USA

Abstract. We investigate shock waves generated by excimer laser ablation of sheet polyimide confined in water. The velocities of the ablation-induced pressure waves in the water are determined by an optical probe system. We measure supersonic velocities up to a few hundred microns away from the irradiated surface, indicating the formation of shock waves. We use these velocities to calculate the corresponding pressures. They are already in the kbar range at fluences comparable to the threshold of ablation. The shock pressure varies as the square root of the incident laser fluence, a behavior that is explained by the rapid heating of the confined gaseous products of ablation.

The initially planar shock waves propagate, become spherical, and decay within a few hundred microns in the surrounding water to acoustic waves. During spherical expansion the shock pressure drops as the inverse of the square of the propagation distance.

The shock waves generated may be relevant in explaining photoacoustic damage observed in biological tissue after excimer-ablation at corresponding irradiances. They may also be important in material processing applications of excimer laser ablation of polymers as they can lead to plastic deformation.

PACS: 81.60.Jw, 43.35.Cg, 87

The ability of the ArF excimer laser to make high precision cuts with thermal damage extending less than 1 µm from the edge of the incision is one of the reasons for the interest in this laser for corneal and keratorefractive surgery. However recent studies of ArF laser ablation of skin in air have shown tissue damage up to 200 µm below the bottom of the incision [1]. Similar results have been found earlier in cornea [2, 3]. For confined ablation of skin in water the damage zone was significantly larger, up to 300 µm [4]. Although these large damage zones have all been attributed to photoacoustic effects, a clear understanding of the underlying damage mechanism is missing. In particular it is unclear whether a shock wave is formed or if the damage is due to strong acoustic waves.

A shock wave differs *qualitatively* from an acoustic pressure transient. It is characterized by a supersonic propagation speed and a very steep front that for all practical purposes can be treated as a discontinuity in pressure, density, particle velocity and internal energy. At the shock front the pressure rises a few kbars within

a distance of a few nanometers, resulting in pressure transients with risetimes of a few picoseconds [5]. A shock also changes the thermodynamic state of the medium in which it propagates in a different way than an adiabatic process does.

Acoustic pressure transients of several hundred bars with risetimes of a few nanoseconds have been observed in excimer ablation of tissue and organic polymers using polyvinylidenefluoride (PVDF) piezoelectric transducers, [6, 7]. However these transducers, because of their limited bandwidth, do not allow detection of the presence or measurement of the peak pressure of shock waves. To date, no direct detection of shock waves in connection with UV excimer ablation has been reported.

In order to study the acoustic effects associated with UV laser ablation we investigated the ablation of a thin (25 µm) sheet of polyimide immersed in distilled water. To ablate the targets we use a XeCl excimer laser emitting at 308 nm, as the high optical absorption coeffecient α_0 of polyimide at that wavelength, $\alpha_0 = 10^5\,cm^{-1}$ [8, 9], makes it a reasonable model for the ablation of tissue

with 193 nm radiation; at that wavelength the absorption coefficient of the cornea has been measured to be 2700 cm^{-1} [10].

Using an optical probe system we measure the velocities of the laser-induced stress waves in the water as a function of incident laser fluence. We measure supersonic velocities, which indicates the formation of shock waves, at fluences close to the threshold of ablation. While it would be desirable to analyze the generated shocks directly inside the polyimide, the optical properties of our targets do not allow this with our setup. However, assuming an acoustic reflection at the interface between the two materials, the characterization of the shock waves in the water gives physical insight into the ablation of polyimide. Our work also suggests that the effects of laser-induced stress waves may be important in patterning microelectronic materials by UV-ablation.

In our experiments the polyimide sheet is completely immersed in water, thus increasing photoacoustic effects by confinement of the ablated material. Because the equation of state of water is known, using jump conditions at the shock front it is straightforward to calculate the peak pressures corresponding to the measured shock velocities. We observe the generation of strong (multi-kbar) shocks in water. We determine how these pressures decay during the expansion of the shocks in the water. In order to find the thresholds for the ablation confined in water and verify that the logarithmic dependence of etch-depth on fluence observed for ablation in air applies [9, 11], we also measure the etch-depth per pulse of the immersed polyimide. At low fluences we find a logarithmic dependence on the incident laser fluence.

Our observations are explained by a simple ideal gas model. We show that shocks develop from the high pressure transient that is generated by the expansion of rapidly heated confined gas.

1 Experimental Methods

Our experimental setup is illustrated schematically in Fig. 1. To ablate our targets we use a XeCl excimer laser (Lambda Physik model EMG 103 MSC) that emits pulses of a duration of 20 ns at a wavelength of 308 nm [12]. A circular aperture of a diameter of 5 mm selects a uniform part of the laser beam that passes various attenuation filters and an aspheric lens with a focal length of 18 mm. The beam is focused through a quartz window into a cuvette that is filled with distilled water prior to the experiment. During the experiment the water is not changed.

As targets we use sheet polyimide of a thickness of 25 μm immersed in water. It is clear that the confinement of the target by liquid has an amplifying influence on the acoustic effects unter investigation. To keep that influence constant the irradiated site was always more than 10 mm below the water surface. Indeed it has been shown in experiments on laser fragmentation of biliary and urinary stones performed at similar irradiation conditions as discussed here that the amplitude of a laser-generated
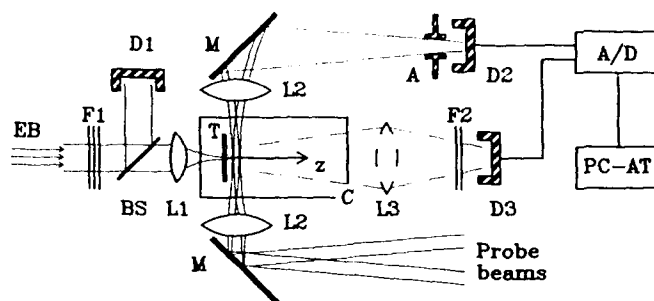

Fig. 1. Schematic view of the experimental setup. The He-Ne probe beams are separated by 35 μm and can be translated in space without changing their relative spatial separation. The target T is mounted on a separate translation stage and can be positioned relative to the probe beams with an accuracy of 10 μm. The z-axis is the axis of the excimer beam EB with $z = 0$ at the rear surface of the target. To determine penetration of the target, the transmitted UV-radiation is collected with lens L3 and imaged onto photodiode D3. C cuvette filled with water, BS beam splitter, M mirror, L_i lenses, D_i detectors, F_1 neutral density filter, F_2 bandpass filter, A aperture, A/D digitizer

stress wave does not depend on the immersion depth, provided that that is larger than 3 mm [13].

To determine the velocity of shock waves propagating in water we use an optical probe technique that was described in detail elsewhere [14]. We focus two TEM$_{00}$ Helium-Neon probe beams into our cuvette in such a way that they are parallel to each other and to the surface of the target. A fast photodiode (EG & G model FND 100, risetime < 1 ns) detects them after they have propagated through an imaging lens and an aperture.

The probe beams have a waist of $\omega_0 = 7$ μm and are laterally separated by a distance of about 35 μm. Their axes intersect the axis of the ablating beam, which is perpendicular to the surface of the target and denoted as the z-axis in Fig. 1. The intersection between the back surface of the target and the z-axis is taken as the origin $z = 0$. $X-Z$-translation stages allow the simultaneous displacement of the two probe beams parallel and perpendicular to the surface of the target. Unless otherwise specified the probe beams are at the back of the irradiated targets.

The pressure waves propagating in the water create density variations and therefore transient changes in the index of refraction. As they traverse the probe beams, these beams are deflected out of the acceptance angle of the detection optics. Because the changes in the index of refraction of the water are small, on the order of a few percent [15], deflection is efficient only near grazing incidence, so that once the pressure wave has moved through the probe beam at its waist, the probe beam is again imaged onto the photodiode. The net result is a decrease of the photodiode signal (D2) for a duration roughly equal to the transit time of the pressure wave through the probe beam, about ten nanoseconds in our setup. Because both probe beams produce the same effect, the photodiode signal consists of two such variations in sequence. The signal is digitized by a Tektronix digitizer (model AD 7912, 750 MHz bandwidth) and sent on a GPIB bus to an IBM-AT-clone computer for analysis. A computer program locates the two peaks of the photodi-

ode signal and allows us to determine their separation to an accuracy of 0.5 ns. That time is the transit time of the pressure wave through the axes of our two probe beams. At sufficiently large distances from the target, the pressure waves become sonic and propagate at the velocity of sound in water of 20°C, $c_s = 1.483$ km/s. Measuring the transit time far away from the target thus allows us to determine the distance between the two probe beams.

In short, our setup allows the non-invasive determination of shock velocities in water to an accuracy of 5%. The spatial resolution is equal to the axial separation of the two probe beams, $\sim 35\,\mu$m. In addition, we can monitor the dynamics of gas bubbles created during ablation by locating the probe beams in front of the target where the ablation takes place. As cavitation bubbles typically expand at velocities of 20-100 m/s, their signals can easily be distinguished from those created by the more than fifteen times faster pressure waves.

When measuring the shock velocities, we changed the targets frequently in order to eliminate the effects of thinning of the target by ablation; at most three laser pulses were fired onto the same surface spot. Every time a fresh spot was irradiated, the target was repositioned carefully relative to the probe beams. This is imperative, as the shock waves transmitted into the water attenuate significantly within a few tens of microns because of geometrical expansion. Ideally the axis of the ablating beam and the two waists of the probe beams should lie in the same plane. The axis of the ablating beam should also intersect the surface of the target and the axes of the two probe beams at a right angle. Moving the target through the probe beams and simultaneously measuring the transmitted light on the photodiode (D2) allows us to position the target to an accuracy of 10 μm.

To determine the etch rate of polyimide immersed in water we measured the number of pulses to penetrate. We added a lens (L3) that images the UV-light transmitted through the sample onto another photodiode (D3) placed behind an UV-bandpass filter to the above setup. Since the optical absorption coefficient α_0 of polyimide at 308 nm is very high, there is no signal from that diode unless the target has been nearly penetrated. It is therefore relatively easy to count the number of pulses necessary to drill through a target sheet of polyimide. Dividing its thickness by that number gives the etch-depth per pulse. We took data from fluences of ~ 100 J/cm² down to ~ 150 mJ/cm². Once the number of pulses to drill through became larger than 5000, corresponding to an etch-depth per pulse of less than 5 nm, we assumed that the fluence was below the ablation threshold and stopped the data acquisition.

The fluence F of the ablating pulse at the surface of the target is calculated from measurements of the pulse energy and the spot size. We reduce the maximum pulse energy of about 4 mJ by a set of attenuating filters (F1) and determine the energy of the ablating pulse by measuring a split-off part of the beam with a pyroelectric detector (D1) (Molectron model J3-09). To obtain the energy deposited into the focal spot, we multiply the measured energy with a transmission factor that corrects for the attenuation of the beam because of reflection at

quartz-air and quartz-water interfaces. The area of the irradiated spot is determined by microscopic examination. It is elliptical with principal axes of 90 and 62 μm and an area $A = 4.4 \times 10^{-5}$ cm². We calculate the fluence $F = E_{in}/A$ by assuming uniform illumination of the focal spot with a laser pulse of energy E_{in}. We work with fluences up to 90 J/cm² corresponding to irradiances up to 4.5 GW/cm².

2 Results

2.1 Shock Wave Measurements

Below a fluence of 8 mJ/cm² we do not obtain any signal with our optical probe-system, neither in front nor in back of the irradiated targets. Starting at that fluence value small gas bubbles form at the irradiated surface. As they scatter a probe beam that illuminates the front surface at grazing incidence, we can detect them with our setup. They may consist of the gases that have been observed to emanate from below the surface of polyimide during ablation in air at very low fluences [16] or simply of water vapor resulting from conductive heating of the water by the irradiated surface of the target. At these low fluences the generated microcavities have lifetimes of about 10 μs. The acoustic transients that they generate are below our detection limit.

At a fluence of $F_0 = 50$ mJ/cm² we begin detecting pressure waves in front of the target. They propagate at a speed about 5% or 75 m/s above the speed of sound. The corresponding pressure transients that are launched into the polyimide are still too small to be detected by our probe system at the back side of the target. Because F_0 is about equal to the threshold of ablation determined in air by photoacoustic techniques (45 mJ/cm² [11, 17]), we conclude that F_0 is the threshold for confined ablation, even though it is smaller than the value F_s determined from the extrapolation of the etch-depth data below (cf. Sect. 2.2).

For fluences between 130 mJ/cm² and about 100 J/cm² we monitor the strength of the transmitted shock waves. During spherical expansion in the water, their velocities drop to the speed of sound after propagation over a distance of a few hundred microns.

We calculate the peak pressures of the shock waves propagating in water from measured shock velocities by using the jump condition,

$$P_s = \varrho_0 U_s u_p, \tag{1}$$

where P_s is the shock pressure, $\varrho_0 = 0.987$ g/cm³ the density of water at 20°C and U_s and u_p the shock and particle velocities. U_s and u_p are further related by the equation of state. To first approximation

$$U_s = a + b u_p, \tag{2}$$

with the values $a = 1.483$ km/s and $b = 2.07$ for water [15].

Shock pressures determined from the measured shock velocities are presented in Fig. 2a, b. Figure 2a shows the dependence of the shock pressure $P_s(z_0, F)$ on the
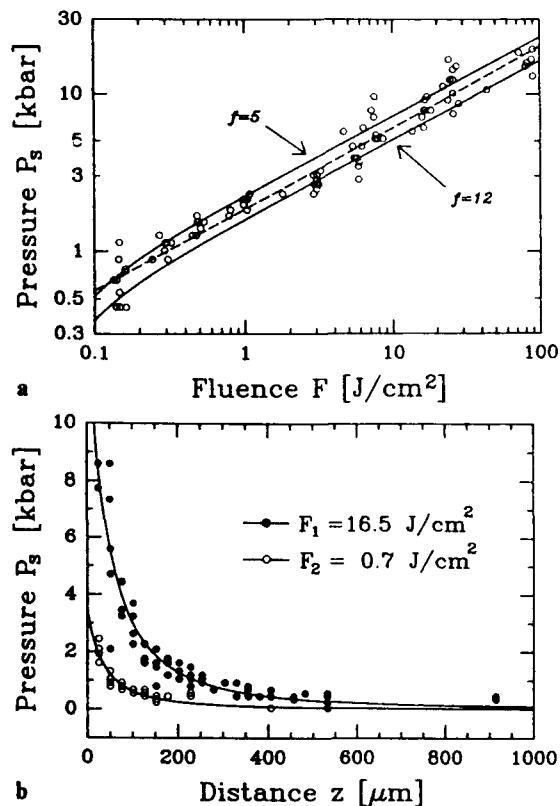
Fig. 2a, b. Shock pressures of the waves transmitted into the water at the rear surface of 25 μm-thick samples were calculated from measured velocities using (1–2). **a** Shock pressure $P_s(z_0, F)$ vs fluence F at $z_0 = 25$ μm (o), 50 μm away from the irradiated surface. The dashed line is a least square fit of the data in double-logarithmic representation. It has a slope of 0.52. The solid lines are predictions of the thermal model explained in the text. They were calculated with (6) assuming the expanding gas to be ideal with a molar specific heat at constant volume, $c_v = (f/2)R$, where f is either 5 or 12. **b** Shock pressure $P_s(z, F_i)$ vs distance z from the rear surface of the target for two fixed laser fluences $F_1 = 16.5$ J/cm^2 (•) and $F_2 = 0.7$ J/cm^2 (o). The solid lines are fitted curves that assume a $1/(z - z_i)^2$ decay according to (3). Such a decay is expected from momentum conservation of the shock front

fluence F of the ablating pulse at the fixed distance $z_0 = 25$ μm away from the rear surface of the target. The pressure data plotted in a double-logarithmic plot are well fitted by a straight line (dashed), implying a power law dependence between the shock pressure and the laser fluence. The least square fit gives a slope of 0.52. At 250 mJ/cm^2, 5 times the threshold of ablation, which is in the typical working range of practical applications, the fit indicates a pressure P_s of 905 bar. The two solid lines in Fig. 2a are theoretical predictions from the ideal gas model discussed in Sect. 3.1. They were calculated by assuming the gas to have a molar specific heat at constant volume c_v of either 5/2 R or 6 R, R being the universal gas constant.

In Fig. 2b we show the decay of the shock pressure with distance z from the rear surface of the target at $z = 0$ as the shock wave propagates into the surrounding water for the two fluences $F_1 = 16.5$ J/cm^2 and $F_2 = 0.7$ J/cm^2. At large enough distances z the shock waves expand spherically, and, because of momentum

conservation, their pressure P_s varies inversely with the square of the distance from the center of the shock [14]. Accordingly we fit the data by:

$$P_s(z, F_i) = P_i \left(\frac{z_0 - z_i}{z - z_i} \right)^2, \tag{3}$$

where P_i and z_i, $i = 1, 2$, are the two parameters of that fit. We obtain numerically $P_1 = 8.3$ kbar and $P_2 = 1.9$ kbar. These values agree well with the data from Fig. 2a, which is expected, as $P_i = P_s(z_0, F_i)$. The other parameter of (3), z_i, indicates where on the z-axis the center of the spherically expanding shock lies. If the ablation-induced shock were always spherical, we would expect the center of shock to lie on the irradiated front surface of the target, $z_i \approx -25$ μm. If it were planar, we would have $z_i = -\infty$. The fitted values, $z_1 = -88$ μm and $z_2 = -75$ μm, are in between, indicating that the generated shocks are initially planar and become spherical only after propagating a few tens of microns.

2.2 Etch-Rate Measurements

At fluences equal to several times the ablation threshold, photo-etching of polyimide at the XeCl laser wavelength of 308 nm is generally well described by a *blow-off model*. In that model one assumes that the radiation attenuates exponentially with distance from the surface into the target according to some effective absorption coefficient α_e, and that all material that absorbs an energy density $\geq \alpha_e F_s$, where F_s is a threshold fluence for *significant* photo-etching, is ablated. The resulting etch-depth d is given by [9, 18, 19]:

$$d = \alpha_e^{-1} \ln \left(\frac{F}{F_s} \right). \tag{4}$$

Our etch-data, shown in Fig. 3 in a semi-logarithmic representation, follows (4) for fluences below about 20 J/cm^2 with the fitted parameter $F_s = 150$ mJ/cm^2 and $\alpha_e = 3.6 \times 10^4$ cm^{-1}. These values are similar to those obtained by other workers for photo-etching of polyimide in air
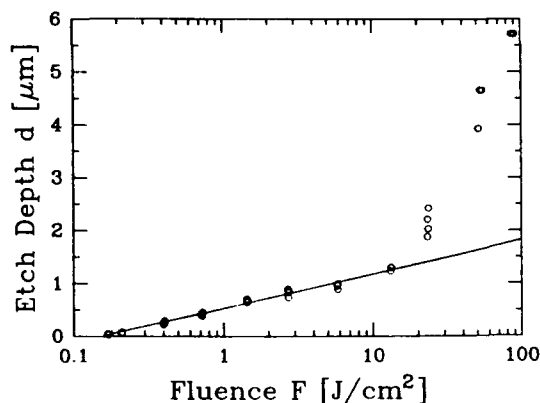

Fig. 3. Etch-depth d vs fluence F for confined ablation of polyimide. The solid line is a fit to the data by (4) for fluences less than 20 J/cm^2. The sharp increase of etch-depth at that fluence is accompanied by permanent mechanical deformation of the target

Table 1. Effective absorption coefficient α_c and threshold of ablation F_s, derived from published data by assuming a blowoff model according to (4). When the data deviated from that dependence at high fluences, only the low-fluence part was used for the fit. Note that α_c is smaller than the low fluence optical absorption coefficient $\alpha_0 = 10^5\,\text{cm}^{-1}$, and that F_s is larger than the threshold fluences determined photoacoustically, $F_0 = 45\,\text{mJ/cm}^2$

Effective absorption coefficient	Threshold fluence	Heat of ablation	Pulse duration	Data from
α_c $[10^4 \times \text{cm}^2]$	F_s $[\text{mJ/cm}^2]$	$\alpha_c F_s$ $[\text{kJ/cm}^3]$	τ $[\text{ns}]$	
3.6	150	5.3	20	This work
4.2	109	4.6	300	[11]
8.4	69	5.8	35	[9]
5.0	101	5.0	17	[25]
5.3	88	4.7	7	[11]
15.4	31	4.8	0.005	[29]

(cf. Table 1), indicating that, at least for low fluences, the etch-depth of polyimide is not influenced by the confinement of the target.

At fluences above $20\,\text{J/cm}^2$ our etch-depth per pulse becomes larger than what (4) predicts and the microscopic appearance of the ablated region is different from that resulting from irradiation a lower fluences: At the front surface the drilled holes are now surrounded by a funnel shaped region of modified surface texture that indents slightly into the target. Width and depth of that region increases with fluence and amount to about $30\,\mu\text{m}$ and $9\,\mu\text{m}$ at $90\,\text{J/cm}^2$; we attribute this to the permanent mechanical deformation of the target by the strong pressure transients.

3 Discussion

3.1 Shock-Pressure

To calculate the generated shock pressures we adapt an ideal gas model used by other workers to explain shock generation from confined ablation of metals [20, 21]. In that picture it is assumed that a constant mass of an ideal gas enclosed by two pistons is heated by a laser pulse. If the expansion of the gas is violent enough to drive shock waves into the pistons, the two confining surfaces of the expanding gas move at the particle velocities of the piston material through which these shock waves have passed. The correct boundary conditions of the expansion of the gas thus follows from the relationship between shock pressure and particle velocity of the confining materials. The resulting peak pressure P_p is given in [20] as:

$$P_p(F) = 0.95 \cdot \left[\frac{ZF}{(1 + f/2)\tau} \right]^{1/2}, \tag{5}$$

where F is the laser fluence absorbed by the gas, τ the duration of the laser pulse, Z an effective shock impedance and $f = 2c_v/R$, c_v being the molar specific heat of the ideal gas and R the universal gas constant.

The factor 0.95 in (5) was derived in a dimensionless numerical analysis of the gas expansion that assumed heating by absorption of a laser pulse of Gaussion time profile.

$Z = Z_1 Z_2/(Z_1 + Z_2)$ is an effective impedance that combines the shock impedances Z_i of the two materials, i.e. the respective products of density and shock velocity. We shall approximate them below by $Z_1 = 30.7\,\text{bar}/(\text{m/s})$ for polyimide [22] and $Z_2 = 14.6\,\text{bar}/(\text{m/s})$ for water, the products of density and adiabatic sound speed. This is common in the approximate theory of traveling waves of finite amplitudes [23].

Note that (5) implies that a constant fraction of the energy that heats the gas is converted into acoustic energy. That fraction depends only on the impedances involved and, through f, on the specific heat of the gas. This follows because the intensity of an acoustic wave is proportional to the square of its pressure.

In thermal coupling measurements it has been found that when irradiating polyimide below a threshold fluence F_0, all the absorbed laser energy E_{in} is converted into heating of the target [17]. At fluences above that threshold the heat deposited in the target remains approximately constant, and the excess energy $E_{in} - AF_0$, A being the area of the irradiated spot and F_0 the threshold fluence of ablation, is carried away by the ablated material [17]. Consequently we modify the above (5) by replacing F by $F - F_0$ as the heat source of the confined gas.

Because of the mismatch of the acoustic impedances at the interface between polyimide and water, the pressure created during ablation at the polyimide surface is higher than the peak pressure of the shock propagating in the water. As the shock passes the material interface, it is only partially transmitted. The shock pressure is reduced by a factor $T_{ac} = 2/(1 + Z_1/Z_2)$, which equals 0.65 in our situation. The shock pressure P_s of the waves propagating into the water at the rear side of the target is then given by the ablation pressure P_p from (5) multiplied by T_{ac}. According we have:

$$P_s(F) = 0.95 \cdot T_{ac} \left(\frac{Z}{1 + f/2} \right)^{1/2} \cdot \left(\frac{F - F_0}{\tau} \right)^{1/2}. \tag{6}$$

In this equation the number f, which is related to the molar specific heat c_v of the gas by $f = 2c_v/R$, is the only parameter that is not well known. If the molecular vibrations are frozen, which is a good approximation at room temperature, f equals the number of translational and rotational degrees of freedom of a gas molecule. f becomes larger at high temperatures where a considerable part of the gas molecules are vibrationally excited. The contribution of each normal vibration of each molecule to the specific heat c_v increases with temperature T, reaching the value $k_B T$ asymptotically, k_B being the Boltzmann constant. Therefore f is equal to or larger than the number of tranlational and rotational degrees of freedom of a molecule and smaller than that number increased by twice the number of vibrational degrees of freedom [24].

The principal gaseous ablation products of polyimide in air are CO, CO_2 and H_2O and elemental carbon [9, 25]. In vacuum, in addition HCN and benzene, which how-

ever may not be a primary ablation product [26], have been detected [9, 25]. In order to describe the gaseous ablation products by a simple ideal gas, admittedly a crude approximation, we consider below the two limiting cases $f = 5$ and $f = 12$. $f = 5$ corresponds to a diatomic or linear polyatomic molecule with frozen vibrations and $f = 12$ follows for a gas consisting of nonlinear tri-atomic molecules, e.g. H_2O, where all the three normal vibrations are contributing the maximum value R to the specific heat. As the principal gaseous ablation products are di- and tri-atomic molecules these two values for f give the extremal predictions of the model for the pressure. As can be seen from (6) they differ by a factor of $\sqrt{2}$.

We take for F_0, the threshold of ablation, the lowest fluence where our probe system detects the emission of pressure waves, $F_0 = 50\,mJ/cm^2$ (cf. Sect. 2.2), and we assume a pulse duration of $\tau = 20\,ns$. Note that the prediction of (6) is of course not sensitive to the exact value of F_0 at high fluences.

The resulting pressure versus fluence dependences corresponding to $f = 5$ and $f = 12$, calculated by (6), are plotted in Fig. 2a as solid lines. Given the simplicity of the model, the congruence of its prediction with the experimental data is remarkable. However in the calculation several simplifications have been made and must be kept in mind. First of all, the calculation assumes a planar shock. The measurement shown in Fig. 2a was at $50\,\mu m$ away from the irradiated surface. That distance is only a little bit less than the small principal diameter of our focal spot, $62\,\mu m$, and edge effects have probably already started to weaken the shock. Also the illumination of the focal spot is not perfectly uniform. Second, the mass of the removed material increases with fluence. The corresponding increase of the separation of the pistons that confine the expanding gas in the model description is equal to the etch depth. In our experiment this varies between 9% and 26% of the piston separation at the end of the laser pulse, which is predicted by the model as $P_p\tau/Z$ [21]. Increasing the piston separation, while keeping the total internal energy constant, reduces the pressure in the gas. As this effect is neglected in the model, the predicted pressures should slightly overestimate the experimental data. Finally, as mentioned above, we assumed in the calculation an ideal gas with either no or three fully excited normal vibrations per molecule.

The pressure of the ablation-induced shock waves during spherical expansion in the water varies as the reciprocal of the square of the distance from the center of the shock. This has been observed earlier for shock waves induced by optical breakdown and explained by conservation of momentum of the shock front [14]. Note however that before spherical expansion becomes important, the shock propagates as a plane wave for a distance that increases with the spot size of the ablating beam.

At an irradiance of $\sim 4.5\,GW/cm^2$ we generate shocks of $\sim 30\,kbar$ inside the polyimide using pulses of 4 mJ. These pressures are comparable to those of shocks generated in confined laser ablation of metal foils. There pressures of about 40 kbar were reported for irradiances of a few GW/cm^2 obtained using laser pulses of a dura-

tion of 30 ns and pulse energies of up to 100 J [21]. Note however that these high-energy laser systems illuminated focal spots of 6 mm diameter, producing extended planar shocks.

3.2 Etch-Depth

It is important to note that (4) fails to describe the etch-depth data near the threshold of ablation [16]. Using quartz crystal microbalances it has been shown that near the threshold of ablation the amount of removed material decreases less rapidly with fluence than predicted by (4) [27, 28]. It was concluded that photo-etching of polyimide at 308 nm is a thermally controlled process, with ablation starting at surface temperatures of about 850° C [28].

Therefore (4), although a good approximation at higher fluences, becomes an inappropriate description of the ablation process very close to threshold. It follows that F_s and α_e, the two parameters of the blow-off model that are calculated by fitting etch-depth to (4), are generally different from the actual ablation threshold F_0 and the optical absorption coefficient α_0. This is confirmed by the values in Table 1. There, for all experiments performed with nanosecond pulses, F_s is larger than the threshold of ablation found photoacoustically and the effective absorption coefficient α_e is smaller than α_0, the optical absorption coefficient determined by transmission measurements at sub-ablative fluences. Note that the experimental data obtained by the different workers are consistent in that the product $F_s\alpha_e$ is always comparable to and larger than $F_0\alpha_0 = 4.5\,kJ/cm^3$.

At fluences higher than $20\,J/cm^2$ our etch-depth per pulse data deviate from (4). We observe permanent mechanical deformation of the target sheets, and the microscopic appearance of the ablated regions changes. Remove Sect. 3.3 from the manuscript: Move the first two sentence of Sect. 3.3 ("At fluences higher than ... the ablated regions changes") as a separate paragraph to the end of Sect. 3.2. Delete the remaining text of Sect. 3.3.

4 Conclusions

The shock waves generated by ablation of polyimide confined in water using 308 nm excimer laser radiation have been studied. The measured shock pressures are proportional to the square root of the fluence of the ablating pulse. This can be explained by a simple thermal model that describes the expansion of a confined ideal gas subjected to rapid heating. According to the model, the ablation pressure depends on irradiance, on the specific heat of the gas mixture created during the ablation and on the acoustic impedances of the target and the confining material.

At fluence $F \geq 300\,mJ/cm^2$, about twice the threshold for *significant* photo-etching, shock pressures of more that 1 kbar are launched into the confining water. Tissue ablation by excimer lasers is usually carried out at similar irradiances. It is therefore likely that true shocks and not just strong acoustic waves are generated in tissue during ablation by laser pulses of a duration of a few nanoseconds or less.

References

1. S. Watanabe, T. Flotte, D. McAucliffe, S. Jacques: J. Invest. Dermatol. **90**, 761 (1988)
2. J. Marshall, S. Trokel, S. Rothery, H. Schubert: Ophthalmol. **92**, 749 (1985)
3. E. Dehm, C. Puliafito, C. Adler, R. Steinert: Arch. Ophthalmol. **104**, 1364 (1986)
4. Y. Yashima, D. McAucliffe, S. Jacques, T. Flotte: Lasers Surg. Med. **11**, 62 (1991)
5. P. Harris, H. Presles: J. Chem. Phys. **77**, 5157 (1982)
6. F. Cross, R. Al-Dhahir, P. Dyer: J. Appl. Phys. **64**, 2194 (1988)
7. P. Dyer, R. Srinivasan: Appl. Phys. Lett. **48**, 445 (1986)
8. H. Philipp, H. Cole, Y. Liu, T. Sitnik: Appl. Phys. Lett. **48**, 192 (1986)
9. J. Brannon, J. Lankard, A. Baise, F. Burns, J. Kaufmann: J. Appl. Phys. **58**, 2036 (1985)
10. C. Puliafito, R. Steinert, T. Deutsch, F. Hillenkamp, E. Dehm, C. Adler: Ophthalmol. **92**, 741 (1985)
11. R. Taylor, D. Singleton, G. Paraskevopoulos: Appl. Phys. Lett. **50**, 1779 (1987)
12. The risetime of our laser pulses is 4 ns. They show an equally fast initial fall that is followed by a pedestal. The intensity is larger than 10% of the peak during a time $\tau = 20$ ns that is taken as the pulse duration
13. P. Teng, N. Nishioka, R. Anderson, T. Deutsch: IEEE J. QE-**23**, 1845 (1987)
14. A.G. Doukas, A.D. Zweig, J.K. Frisoli, R. Birngruber, T.F. Deutsch: Appl. Phys. B (in press)
15. P. Harris, H. Presles: J. Chem. Phys. **74**, 6864 (1981)
16. R. Srinivasan, K. Casey, B. Braren, M. Yeh: J. Appl. Phys. **67**, 1604 (1990)
17. P. Dyer, J. Sidhu: Appl. Phys. **57**, 1420 (1985)
18. T.F. Deutsch, M. Geis: J. Appl. Phys. **54**, 7201 (1983)
19. J. Andrew, P. Dyer, D. Forster, P. Key: Appl. Phys. Lett. **43**, 717 (1983)
20. R. Griffin, B. Justus, A. Campillo, L. Goldberg: J. Appl. Phys. **59**, 1968 (1986)
21. R. Fabbro, J. Fournier, P. Ballard, D. Devaux, J. Virmont: J. Appl. Phys. **68**, 775 (1990)
22. The adiabatic sound speed of polyimide was calculated from PVT-data supplied by the manufacturer. Note that this calculated value, $c_0 = 2165$ m/s, is but a first approximation, as sheet polyimide is not an isotropic material
23. D. Blackstock: In: *American Institute of Physics Handbook*, ed. by D. Gray (American Institute of Physics, McGraw-Hill, New York 1982) pp. 3-190
24. G. Herzberg: *Molecular spectra and molecular structure II. Infrared and Raman spectra of polyatomic molecules* (van Nostrand, Princeton, NJ 1968) pp. 501-519
25. R. Srinivasan, B. Braren, R. Dreyfus: J. Appl. Phys. **61**, 372 (1987)
26. J. Yeh: J. Vac. Sci. A **4**, 653 (1986)
27. S. Lazare, V. Granier: J. Appl. Phys. **63**, 2110 (1988)
28. S. Küper, J. Brannon: In: *Technical Digest, Conference on Lasers and Electro-Optics*, Paper CFF2 (Optical Society of America, Washington D.C. 1991) pp. 506-508
29. B. Nikolaus: In: *Technical Digest, Conference on Lasers and Electro-Optics*, pages Paper TUJ2, (Optical Society of America, San Francisco, SA 1986) pp. 88-89

A thermo-mechanical model for laser ablation

A. D. Zweig

Wellman Laboratories of Photomedicine, Massachusetts General Hospital, Boston, Massachusetts 02114

A steady-state model for ablation of materials by strongly absorbed long-pulse lasers is developed. Material is removed by a combination of evaporation and ejection of liquid due to evaporation-induced pressure gradients at the bottom of the ablation crater. The relative strength of the two processes depends on the details of the liquid flow. An explicit expression for the drilling velocity is derived. The model explains experimental drilling-depth and recoil data. It is applicable to materials that melt and vaporize.

I. INTRODUCTION

Drilling depth and target recoil provide important and easily measurable information on laser ablation. They vary with distance between the surface of the target and the laser beam waist. For pulses of several 100-μs duration, the observed variation is very similar for tissue, gelatin, and metals, suggesting that the same physical mechanisms are involved when ablating these materials.[1,2]

Modeling ablation by evaporation and ejection is not a new idea, but has long been used to describe laser ablation of metals[3-5] and, more recently, of biological targets.[6,7] Here, I will show how a model based on such an approach indeed explains the experimentally observed dependence of drilling depth and recoil momentum on waist-surface distance. The concept is equally well applicable to metals and biological targets, since these two types of target materials differ primarily in the physical mechanism that determines the depth of energy deposition. In metals it is heat conduction, while in tissue it is the absorption of radiation. The ablation of gelatin by pulsed Er^{3+}:YAG laser radiation, whose wavelength, 2.94 μm, corresponds to the peak of the water absorption in the infrared, will be used to illustrate the model.

The steady-state model describes ablation of materials by strongly absorbed laser radiation. It neglects heat conduction and assumes that the optical penetration depth of the radiation is small compared to the spot diameter of the drilling beam. Attention will be given to the influence of the spot size on the ablation mechanism. The drilling pulses are assumed to last 100 μs or longer, corresponding to pulsed emission of free-running solid-state lasers and axial-flow CO_2 lasers. The model assumes irradiances well above threshold, so that a strong vaporization develops instantaneously at the target surface. The radial gradient of the evaporation-induced pressure on the target surface causes the displacement and eventual ejection of liquified material. This increases the drilling efficiency and affects the recoil of the target induced by the gaseous and liquid ejecta.

Note that the model assumes the formation of a liquid layer at the surface of the target during ablation. It therefore describes the ablation of materials that form a molten phase before vaporization. It does not apply to ablation by photochemical mechanisms in which the products are formed directly by decomposition of the target, for example, the ablation of some polymers by UV light.

First, a description of the laser-induced evaporation will be given, assuming the formation of a Knudsen layer at the target surface and taking into account the effect of atmospheric pressure.[8] Then, the effect of radial pressure gradients on a thin surface layer will be modeled by solving the corresponding Navier–Stokes equations for steady-state linear flow explicitly. The subsequent analysis leads to an explicit expression for the drilling velocity. The drilling depth is then calculated by numerical integration of the drilling velocity and compared to published experimental data. Finally, the relationship between drilling depth and recoil momentum is discussed.

II. EVAPORATION

The rapid surface evaporation due to absorption of intense laser radiation has been modeled by various authors.[8-11] It occurs whenever the absorbed energy density is much greater than the amount necessary to evaporate the target material.

The description of Knight[8] shall be used in this work, since it considers evaporation into an outside atmosphere rather than into vacuum. The inclusion of the outside atmosphere leads to an enhancement of the forces induced by the evaporated material onto the target surface, as one might intuitively guess. Knight's description assumes a quasiequilibrium evaporation from a plane liquid-vapor interface, the evaporation front, into air at ambient conditions. The model considers a Knudsen layer extending some molecular mean free paths from the liquid into the vapor region.[12] It assumes a discontinuous change of temperature T, pressure p, and density ρ across the evaporation front. The flow of the expanding hot vapor, which drives a shock wave into the surrounding air, determines the strength of these discontinuities. They are given in Ref. 8 as

$$\frac{T_v}{T_s} = \left[\sqrt{1 + \pi \left(\frac{m}{2} \frac{\gamma - 1}{\gamma + 1} \right)^2} - \sqrt{\pi} \frac{m}{2} \frac{\gamma - 1}{\gamma + 1} \right]^2, \quad (1)$$

$$\frac{\rho_v}{\rho_s} = \sqrt{\frac{T_s}{T_v}} \left[\left(m^2 + \frac{1}{2} \right) e^{m^2} \text{erfc}(m) - \frac{m}{\sqrt{\pi}} \right]$$
$$+ \frac{1}{2} \frac{T_s}{T_v} [1 - \sqrt{\pi} m e^{m^2} \text{erfc}(m)], \tag{2}$$

$$m = M_v \sqrt{\frac{\gamma}{2}}, \tag{3}$$

where the subscript v denotes the variables describing the vapor adjacent to the Knudsen layer and s the saturated water vapor. $\gamma = c_p/c_v$ stands for the ratio of heat capacities. M_v denotes the flow Mach number of the vapor leaving the Knudsen layer. Sonic flow applies for the case of evaporation into vacuum.[9] For evaporation into an outside atmosphere, the flow is sonic only if the incident laser fluxes are high enough. Then M_v equals 1, while for subsonic flow it follows from Ref. 8 as

$$\frac{p_s}{p_a} = \frac{\rho_s}{\rho_v} \frac{T_s}{T_v} \left\{ 1 + \gamma M_v \frac{a_v}{a_a} \left[\frac{\gamma_a + 1}{4} M_v \frac{a_v}{a_a} \right. \right.$$
$$\left. \left. + \sqrt{1 + \left(\frac{\gamma_a + 1}{4} M_v \frac{a_v}{a_a} \right)^2} \right] \right\}. \tag{4}$$

Here, γ_a, p_a, and a_a denote specific heat ratio, ambient pressure, and sound speed in air; $\gamma_a = 1.4$ and $a_a = \sqrt{\gamma_a R_a T_a}$, where $R_a = \mathcal{R}/\mathcal{M}_a$; $\mathcal{R}$ is the universal gas constant, and $\mathcal{M}_a$ is the molecular weight; $\mathcal{M}_a = 29$ g/gmol for air. Further, the sound speed in water vapor, $a_v = \sqrt{\gamma R_w T_v}$, is calculated using $\gamma = \frac{4}{3}$ and $\mathcal{M}_w = 18$ g/gmol.

Equations (1)–(4) contain eight unknowns: pressure p, temperature T, and density ρ, for saturated and expanding vapor, plus the Mach flow numbers m and M_v. With the aid of the equation of state, $p = \rho R T$, for saturated and expanding vapor, these variables can all be expressed as a function of the saturated vapor pressure p_s and temperature T_s. These two variables are related by a Clausius–Clapeyron relationship as

$$p_s = A e^{-T_*/T_s}. \tag{5}$$

A and T_* were determined by fitting published vapor pressure data of water with Eq. (5) (Ref. 13); using the values $A = 3.0705 \times 10^5$ bars and $T_* = 4688.2$ K, Eq. (5) fits the data in the range from 120 °C to the critical temperature $T_c = 374$ °C, with an accuracy better than 2%.

Energy balance at the evaporation front provides the missing equation to determine the thermodynamic state of the saturated vapor. To formulate it I introduce the variable I_{evap} as the part of the laser irradiance I_{in} that is actually used to evaporate target material. The relationship between I_{evap} and I_{in} will be discussed below. The location of the liquid-vapor interface is denoted by $D(t)$. The velocity with which it moves into the target as a consequence of evaporative mass removal will be referred to as the thermal drilling velocity $\dot{D}_r$. Using this notation, the energy balance for a small volume fixed at the evaporation front, at $z = D(t)$, reads

$$I_{\text{evap}} + \rho_l \dot{D}_t H_l = \rho_v M_v a_v \left(H_v + \frac{\gamma}{2} (M_v a_v)^2 \right), \tag{6}$$

where the specific enthalpy $H = \epsilon + p/\rho$, ϵ being the internal energy, has been introduced. Note that energy is added to the small volume not only by the laser beam, but also by the transport of the internal energy of the liquid into it, represented by the second term on the left side of Eq. (6). Using mass conservation $\rho_l \dot{D}_t = \rho_v M_v a_v$ across the evaporation front, the energy balance is rewritten as

$$I_{\text{evap}} = \rho_l \dot{D}_t H_{lv}, \tag{7}$$

where the notation has been further simplified by introduction of $H_{lv}(T_v) = (H_v - H_l) + \gamma M_v^2 R_w T_v/2$. In this sum the enthalpy difference $H_v - H_l$ is much larger than the kinetic-energy term. For an initial temperature of 20 °C, one calculates, using published data,[14] $H_v - H_l = 2.630 \pm 0.088$ kJ/g and $H_{lv} = 2.73 \pm 0.1$ kJ/g in the temperature range from 90 to 340 °C.

To connect Eq. (7) with the saturated vapor pressure p_s, I write the equation of state of the saturated vapor in the form

$$p_s = \frac{1}{\gamma M_v} \rho_v \frac{\rho_s}{\rho_v} M_v \sqrt{\gamma R_w T_s} \sqrt{\frac{T_s}{T_v}} \sqrt{\gamma R_w T_v}. \tag{8}$$

Using mass balance across the evaporation front together with the energy balance equation (7), this gives

$$p_s(I_{\text{evap}}) = \frac{I_{\text{evap}}}{H_{lv}} \frac{1}{\gamma M_v} \sqrt{\gamma R_w T_s} \frac{\rho_s}{\rho_v} \sqrt{\frac{T_s}{T_v}}. \tag{9}$$

The force per area p_0 that acts on the surface of the liquid is obtained from momentum conservation across the evaporation front. It is equal to the momentum flux of vapor from the Knudsen layer, $p_s(\rho_v/\rho_s)(1 + \gamma M_v^2)$. Using the equation of state of the vapor and Eq. (9) gives

$$p_0(I_{\text{evap}}) = \frac{I_{\text{evap}}}{H_{lv}} \sqrt{\gamma R_w T_s} \sqrt{\frac{T_v}{T_s}} \frac{1}{M_v} \left(M_v^2 + \frac{1}{\gamma} \right). \tag{10}$$

Note that here the momentum of the liquid relative to the moving evaporation front, $\rho \dot{D}_t^2$, has been neglected. The force acting on the surface thus becomes a product of the evaporated mass per unit time, the sound speed in saturated vapor, and the expression $\sqrt{T_v/T_s}(M_v^2 + 1/\gamma)/M_v$ that is dominated by its dependence on the Mach number M_v. For water at an initial temperature of 20 °C and a 1-atm back pressure, sonic flow applies for surface temperatures $T_s > 223$ °C. Numerically, one then finds $\sqrt{T_v/T_s}(M_v^2 + 1/\gamma)/M_v = 1.578$.

For high enough irradiances, $I_{\text{evap}} \geq 10^5$ W/cm², the pressure p_0 is proportional to I_{evap}. It is therefore useful to define the proportionality factor f_{ev} as

$$f_{\text{ev}}(I_{\text{evap}}) = p_0/I_{\text{evap}}. \tag{11}$$

It is plotted in Fig. 1(a) as a function of I_{evap}, the part of the laser irradiance that is used for evaporation. The variation of f_{ev} is mainly caused by the changing Mach number M_v and is pronounced only at irradiances smaller than 10^5 W/cm².
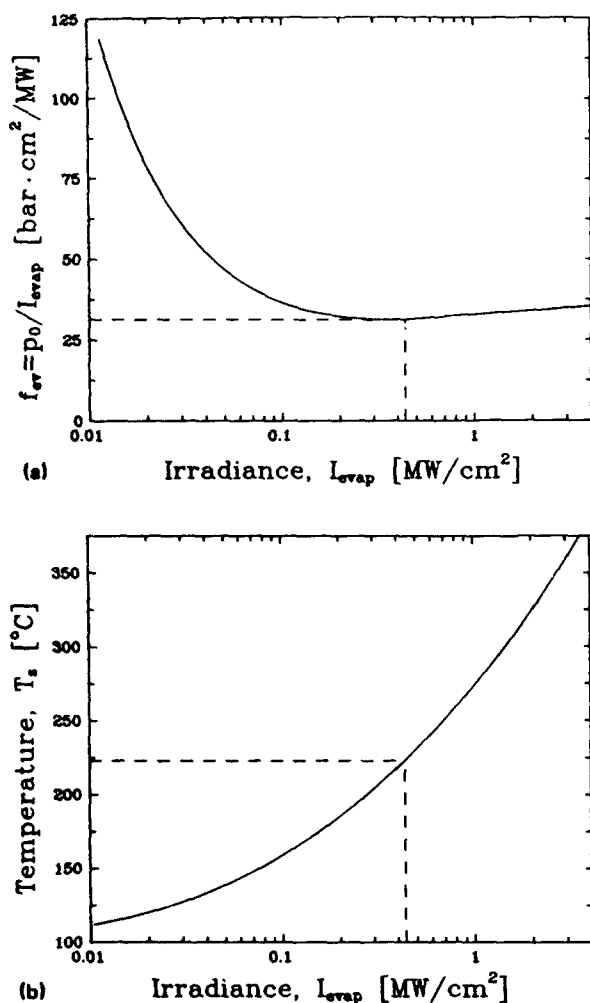
FIG. 1. Description of pure evaporation as a function of the irradiance spent on evaporation, I_{evap}. The target is assumed to be water at normal conditions. The onset of sonic flow at $I_{evap} = 0.44$ MW/cm^2 is indicated by dashed lines. (a) Ratio of pressure acting on the target surface and irradiance spent on evaporation, $f_{ev} = p_0/I_{evap}$, vs I_{evap}. The drop of the curve at low irradiances is mainly due to the changing Mach number. (b) Saturated vapor temperature T_s vs I_{evap}. T_s varies very roughly logarithmically with irradiance. Sonic flow applies for $T_s \gtrsim 223$ °C.
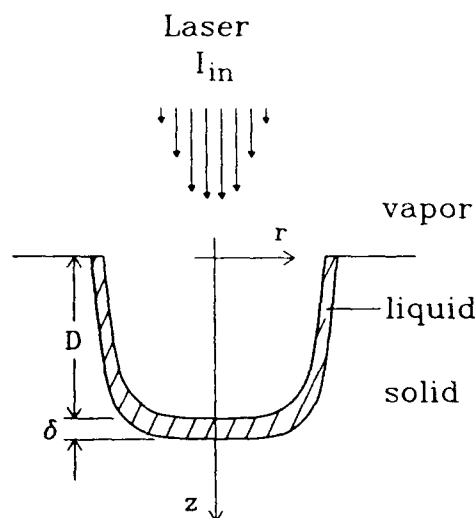

FIG. 2. Illustration of the drilling mechanism. Between vapor and solid a liquid layer of thickness δ forms. The induced material flow enhances drilling. At the center of the crater, radial flow is a good approximation.

Because of the exponential dependence in Eq. (5), the temperature T_s depends approximately logarithmically on the irradiance I_{evap}. This is plotted in Fig. 1(b) for temperatures below the critical temperature of water, $T_c = 374$ °C.

III. EJECTION

The preceding analysis of evaporation assumed a constant irradiance beam profile. In what follows, a TEM$_{00}$ laser beam is assumed. To describe this I apply the results obtained above locally. This is a reasonable approximation for describing the drilling velocity, because the Knudsen layer is very thin compared to the focal spot size, and for the case of sonic flow, which occurs at high enough incident irradiances, the determination of the surface conditions is independent of the exterior vapor flow.

As the pressure p_0 increases monotonically with the irradiance I_{evap}, spatial variations of the Gaussian beam intensity generate radial pressure gradients acting on the irradiated surface. If the shear forces generated within that surface layer are stronger than the shear strength of the material in that layer, it will be displaced radially (cf. Fig. 2). This can be expected if vaporization of the target material is preceded by liquefaction, as is assumed here. The resulting liquid flow is determined by the evaporation-induced radial pressure gradient as well as by the thickness and viscosity of the liquid layer. At the bottom of the crater, the material is displaced predominantly in radial direction. The crater walls deflect the flow into axial direction. This eventually leads to the observed expulsion of liquid from the drilled holes. The generation of a liquid layer thus enhances—and complicates—the ablation process considerably.

A. The thickness of the liquid layer

The thickness of the liquid layer that separates solid from gas at the evaporation front depends on the depth of energy deposition. For ablation of gelatin by infrared radiation, this is determined by the optical penetration depth rather than by heat conduction. Indeed, the typical distance δ_c over which conduction acts is $\sqrt{\kappa t_c}$, $\kappa = 1.44 \times 10^{-3}$ cm^2/s being the heat diffusivity for water. The time t_c during which conduction acts equals roughly the time it takes to ablate a layer of thickness δ_c, i.e., the thickness δ_c divided by the drilling velocity $\dot{D}$. Thus, if the layer thickness during ablation was due to heat conduction alone, $\delta_c = \kappa/\dot{D}$, less than about 0.1 μm for drilling velocities larger than 1 m/s. Compared with the minimal optical penetration depth of water in the IR, $d = 0.75$ μm,[15,16] this is indeed negligible. Note that for metals this is not so; for liquid aluminum and a drilling velocity of 1 m/s, one calculates $\kappa/\dot{D} = 39$ μm, which is much more than the optical penetration depth.
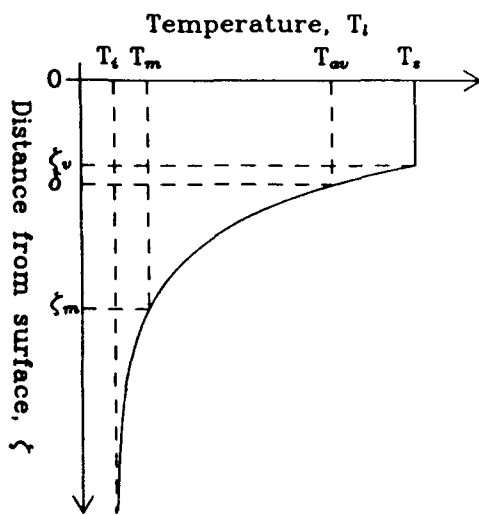
FIG. 3. Illustration of the temperature distribution T_l caused by irradiation of the surface of the target at $\zeta = 0$ from above [cf. Eq. (13)]. Close to the surface T_l is clamped at T_s, the saturated vapor temperature. Deeper inside the target, it drops off exponentially with ζ, the distance from the surface.

The extension of the liquid layer can be calculated approximately by applying energy balance to an infinitesimal volume element at a fixed distance $\zeta = z - D(t)$ away from the evaporation front. In case of pure evaporation, no radial material flow exists. Then, the energy balance near the solid-liquid boundary reads

$$\dot{D}\rho_l c_l\left(-\frac{\partial T}{\partial \zeta}\right) = \frac{\partial I_{evap}}{\partial \zeta}, \tag{12}$$

where $\rho_l = 1$ g/cm³ and $c_l = 4.18$ J/(g K) are the density and specific heat of the liquid, the values for water being assumed.

Assuming the radiation I_{evap} to decay exponentially with a penetration depth d, the temperature of the liquid, T_l is calculated for an initial temperature $T_i = 20$ °C as

$$T_l(\zeta) - T_i = T_s - T_i, \text{ for } 0 < \zeta < \zeta_v,$$

$$= \frac{I_{evap}}{\dot{D}\rho_l c_l}e^{-\zeta/d}, \text{ for } \zeta > \zeta_v \tag{13}$$

The resulting temperature distribution is plotted in Fig. 3. For temperatures below the saturated vapor temperature T_s, T_l decreases exponentially with the distance from the surface, ζ. T_l is equal to the melting temperature T_m at a distance ζ_m away from the surface and to T_s, at another distance ζ_v. In this description the liquid temperature T_l cannot rise higher than T_s at distances closer to the surface, $\zeta < \zeta_v$. The excess absorbed energy in that region is assumed to be spent entirely on the liquid-vapor phase transition.

With the aid of Eq. (7), I obtain from the above Eq. (13):

$$\zeta_m = d \ln \frac{H_{lv}}{c_l(T_m - T_i)}. \tag{14}$$

This expression for the liquid-layer thickness was derived assuming purely evaporative drilling. In the case to be considered, where ejection of liquid increases the ablation speed, the actual temperature decay will be steeper and the resulting thickness of the liquid layer somewhat smaller than ζ_m, the prediction of Eq. (14). However, in view of the logarithmic dependence, the associated changes are small.

The liquid flow also depends strongly on the kinematic viscosity of the molten target material, which for gelatin is difficult to access experimentally above 100 °C, as at these temperatures it decomposes within a few minutes. Around 100 °C I have measured the viscosity and found that it varies about exponentially with temperature, as $\nu(T) = \nu_0 \exp[-\nu_l(T - \vartheta)]$. I shall apply this approximation to extrapolate the viscosity of gelatin to higher temperatures. To calculate the drilling depth in gelatin containing 0.84 g/cm³ water numerically, I shall use below $\nu_0 = 0.11$ cm²/s, $\nu_l = 0.0513$ °C⁻¹, and $\vartheta = 97.5$ °C (cf. Sec. IV).

To simplify the subsequent analysis of the flow, I shall assume that the temperature inside the liquid layer is equal to some average value $T_{av} = T_i + \alpha_{av}(T_s - T_i)$. The parameter α_{av} compares the average rise of temperature of the displaced liquid to the one at the surface of the target. It depends on the axial profiles of temperature and radial flow velocity within the liquid. Here, it will be assumed that α_{av} is constant.

Correspondingly, the thickness δ of the liquid layer is approximated as (cf. Fig. 3)

$$\delta = d \ln \frac{H_{lv}}{c_l \alpha_{av}(T_s - T_i)}. \tag{15}$$

For the experimental situation in mind, the liquid layer δ has a thickness of about 1.5 optical penetration depths or 1.1 μm. Note that in this approximation the viscosity within the liquid layer becomes equal to an average value, independent of ζ.

B. The ejection mechanism

The laser-induced pressure gradients at the evaporation front push material radially outward, away from the axis of the drilling beam. The displaced material can then either flow along the walls and out of the crater, as observed with targets that deform during ablation, remain trapped within.[7] Either way, as long as the displaced material does not obstruct the central part of the beam, the drilling velocity at the center of the drilled hole increases. The total velocity of the evaporation front into the target, $\dot{D}$, thus becomes the sum of two contributions: a thermal drilling velocity caused by evaporation, $\dot{D}_r$ and a mechanical drilling component caused by material displacement, $\dot{D}_m$. Its dependence on the irradiance of the drilling beam will now be discussed.

To describe the liquid flow, I assume that the liquid layer is planar and its thickness small compared to the beam waist ω_0 of the drilling beam. The Navier–Stokes equations then take the form of boundary-layer equations:

$$\frac{\partial v_r}{\partial t} + v_r \frac{\partial v_r}{\partial r} + v_z \frac{\partial v_r}{\partial z} = -\frac{1}{\rho_l}\frac{\partial p}{\partial r} + v\frac{\partial^2 v_r}{\partial z^2}, \qquad (16)$$

$$0 = \frac{\partial p}{\partial z}, \qquad (17)$$

where v_r and v_z denote the radial and axial flow velocities. The continuity equation for cylindrical flow is

$$0 = \frac{\partial v_r}{\partial r} + \frac{1}{r}v_r + \frac{\partial v_z}{\partial z}. \qquad (18)$$

Dimensional analysis shows that the two nonlinear terms in the Navier–Stokes equation (16) have the same order of magnitude. They can be neglected if $v_r\partial v_r/\partial r \ll v\partial^2 v_r/\partial z^2$, which is correct for slow enough flow, i.e., $v_z \ll v/\delta$.

Steady-state flow determines the resulting hole depth, provided that it develops within a time t_s that is short compared to the laser-pulse duration. For pulse durations longer than 100 μs, this is the case, as can be seen from dimensional considerations. Indeed, if one assumes that all the contributions in Eq. (16) are the same order of magnitude, comparing the acceleration term with the viscosity term gives $v_r/t_s \simeq vv_r/\delta^2$ or $t_s \simeq \delta^2/v$. Introducing the appropriate numbers for gelatin at 100 °C, $t_s \simeq 0.1$ μs.

I therefore proceed to solve the linearized steady-state Navier–Stokes equations

$$0 = -\frac{1}{\rho_l}\frac{\partial p}{\partial r} + v\frac{\partial^2 v_r}{\partial z^2}, \qquad (19)$$

$$0 = \frac{\partial p}{\partial z}. \qquad (20)$$

As these equations are linear, one can easily solve for the flow velocities in a moving coordinate system, setting $\zeta = z - D(t)$ (compare Fig. 2). At the liquid-solid interface $\zeta = \delta$, no radial flow is allowed, implying $v_r(\zeta = \delta) = 0$. At $\zeta = 0$, the free surface of the liquid, the correct boundary condition is

$$p = p_0, \qquad (21)$$

$$v\frac{\partial v_r}{\partial \zeta} = 0, \qquad (22)$$

where p_0 is the evaporation-induced pressure, given by Eq. (10). The axial flow velocities at the phase interfaces do not vanish. In the moving frame of reference, they are $v_z(\zeta = 0) = -\dot{D}_t$ and $v_z(\zeta = \delta) = -(\dot{D}_t + \dot{D}_m)$.

The solution to this flow problem is

$$v_r(r,\zeta) = -\frac{1}{2\rho_l v}\frac{\partial p_0}{\partial r}(\delta^2 - \zeta^2). \qquad (23)$$

I can now give an expression for $\dot{D}_m$, the mechanical contribution to drilling. Integrating the equation of continuity (18) gives

$$v_z(r,\zeta) = v_z(r,0) - \left(\frac{1}{r} + \frac{\partial}{\partial r}\right)\int_0^\zeta v_r(r,\zeta')d\zeta'. \qquad (24)$$

Using the above boundary conditions and Eq. (23), this integration is easy. It follows that

$$\dot{D}_m = -\frac{\delta^3}{3\rho_l v}\lim_{r\to 0}\left[\left(\frac{1}{r}+\frac{\partial}{\partial r}\right)\frac{\partial p_0}{\partial r}\right]. \qquad (25)$$

Dimensional analysis of Eq. (25) shows that the mechanical drilling velocity increases with growing layer thickness δ, decreasing viscosity v, or increasing radial surface pressure gradient roughly as $\dot{D}_m \simeq p_0\delta^3/(\rho_l v\omega_0^2)$. This result differs from Eq. (15) in Ref. 6 by the dimensionless factor δ/ω_0. The difference arises because in Eq. (12) of that paper the expression used for the frictional force is erroneous.[17] Nevertheless, the general conclusions drawn there remain valid.

Equation (25) remains accurate as long as the linear approximation holds, i.e., $v_z \ll v/\delta$. As the axial flow velocity v_z is of the same order of magnitude as the drilling velocity, the linear approximation is accurate for small drilling velocities only. For $\dot{D} > v/\delta$, Eq. (25) is but an upper limit to the mechanical drilling velocity. The nonlinear inertia terms in the Navier–Stokes equations (16) and (17) lead to a smaller steady-state mechanical drilling velocity $\dot{D}_m$ as they add resistance to the flow. It can be shown that for highly nonlinear flow the steady-state drilling velocity is given by $\dot{D}_m \simeq 4(\delta/\omega_0)\sqrt{p_0/\rho_l}$. This description of the drilling mechanism then becomes equivalent to the one given by von Allmen[4] that was based on thermodynamic arguments alone. It is interesting to note that, as p_0 is about proportional to I_{evap}, the mechanical drilling velocity $\dot{D}_m$ scales differently with I_{evap}, the irradiance used for evaporation, in the two liquid-flow regimes.

Independent of the details of the flow, the mechanical contribution to drilling increases as the spot size is reduced. Note, however, that this increase is limited by energy conservation, because as the liquid flow carries more heat out of the irradiated region, less energy will be available for the liquid-vapor phase transition. As a consequence evaporation, the driving mechanism of ejection, lessens and the surface temperature T_s drops.

The drilling velocity $\dot{D}$ can be calculated with the aid of Eqs. (7), (11), and (25) once the dependence of the irradiance consumed by evaporation, I_{evap}, on the incident irradiance I_{in} has been established. To this end I consider the energy balance for a small volume centered on axis:

$$I_{in} = I_{evap} + \rho c \alpha_{av}(T_s - T_i)\dot{D}_m. \qquad (26)$$

Because $\dot{D}_m$ depends on derivatives of the pressure p_0, Eq. (26) is actually a differential equation. To obtain an approximate solution, I assume $I_{evap}(r)$ to be proportional to $I_{in}(r)$, the incident irradiance. This assumption is, obviously, the more accurate the smaller $\dot{D}_m$. Now for a Gaussian beam, the mechanical drilling velocity is calculated from Eqs. (11) and (25) as

$$\dot{D}_m = \frac{8}{3}\frac{\delta^3}{\rho_l v\omega^2}\left[I_{evap}\left(f_{ev} + I_{evap}\frac{\partial f_{ev}}{\partial I_{evap}}\right)\right]\Big|_{r=0}, \qquad (27)$$

and $I_{evap}(r = 0)$ follows numerically from Eq. (26). Note that for $I_{evap} \gtrsim 0.1$ MW/cm^2 the proportionality factor f_{ev} is about constant and, therefore, the mechanical drilling velocity proportional to p_0 [cf. Fig. 1(a)].

It is useful, at this point, to simplify the notation by introduction of the drilling velocity ratio φ and the energy consumption parameter ψ as

$$\varphi = \dot{D}_m / \dot{D}_p \qquad (28)$$

$$\psi = \frac{c\rho_{av}(T_s - T_i)}{H_{lv}}. \qquad (29)$$

The drilling velocity ratio φ describes the hydrodynamic aspect of ablation. For linear flow it follows from Eqs. (7) and (25). Its variation with I_{evap} is mainly caused by the strong temperature dependence of the viscosity and, for subsonic gas flow, by the influence of the Mach number on the proportionality factor f_{ev}. The consumption parameter ψ compares the cost of the two drilling processes in terms of energy. It depends but weakly on the irradiation conditions.

Using this notation, I solve Eqs. (7) and (26) for $\dot{D}_t$ to obtain the total drilling velocity

$$\dot{D} = \frac{1}{\rho_l} \frac{I_{in}}{H_{lv}} \frac{1 + \varphi}{1 + \varphi \psi}. \qquad (30)$$

As $\psi < 1$, the drilling velocity grows monotonically with the drilling velocity ratio φ. If ejection becomes dominant, $\varphi \gg 1$, the drilling velocity $\dot{D}$ approaches the value $I_{in}/[\rho_l c \rho_{av}(T_s - T_i)]$. This still depends implicitly on φ, because the amount of energy spent on the liquid-vapor phase transition determines the temperature T_s even if that energy is negligible when compared to the heat carried away by the flowing liquid.
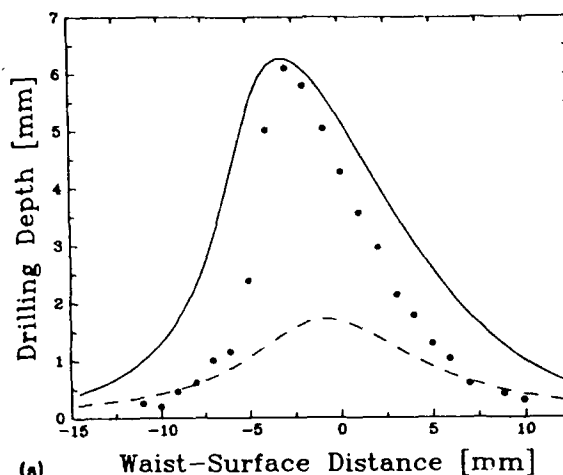
IV. DISCUSSION

In this section the model will be used to discuss drilling depth and recoil momentum, two physical parameters that yield important information on the drilling mechanism. They both depend on the initial position D_0 of the target surface with respect to the beam waist in a characteristic way that is qualitatively very similar for metals and biological targets.[1,2,18]
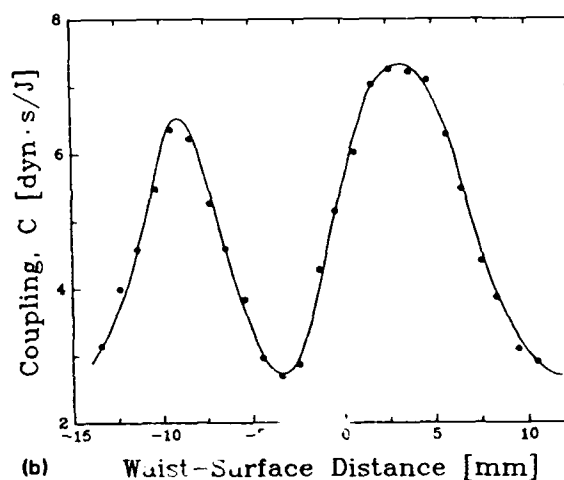
Published measurements, obtained from ablation of gelatin containing 0.84 g/cm^3 water with single Er^{3+}:YAG laser pulses at a wavelength of $\lambda = 2.94$ μm, will now be discussed in detail. In these experiments a TEM$_{00}$ beam with a beam waist of $\omega_0 = 72$ μm and a peak irradiance of 2.45 MW/cm^2 was used. The laser pulses had a duration of $\tau = 200$ μs and a pulse energy of $E_{in} = 40$ mJ. These parameter values will be assumed in the following. Note that the peak fluences used in these experiments, ~ 490 J/cm^2, are much larger than the threshold value for ablation, which for gelatin is similar to guinea pig skin, ~ 1 J/cm^2.[19]

A. Drilling depth

If the experimentally determined drilling depth D_r is small compared to the confocal length $z_0 = \pi \omega_0^2 / \lambda$ of the focused laser beam, the irradiation conditions at the evaporation front do not change during ablation. The resulting drilling depth D_r then just equals the drilling velocity $\dot{D}$

(a)

(b)

FIG. 4. Influence of the distance between the surface of the target and the beam waist on the drilling mechanism. Positive (negative) distance values correspond to a beam waist position located outside (inside) the target. Experimental data from drilling gelatin targets containing 0.84 g/cm^3 water with single laser pulses is denoted by solid circles (●) (from Ref. 1). The corresponding laser parameters were $\lambda = 2.94$ μm, $\tau = 200$ μs, $\omega_0 = 72$ μm, and $E_{pulse} = 40$ mJ. (a) Drilling depth vs waist-surface distance. Drilling depth predicted by the model using $\alpha_{av} = 0.75$ (solid). For comparison the calculated drilling depth in case of pure evaporation is also shown (dashed). (b) Recoil momentum vs waist-surface distance. The line is to guide the eye. The relative minimum of the recoil is observed at the same initial waist-surface distance as the maximum of the drilling depth. This is a consequence of minimizing the amount of evaporated mass.

multiplied by the pulse duration τ. Under tight focusing conditions, however, it is quite common to drill to depths comparable with or larger than the confocal length. In that case the drilling velocity changes with the irradiance at the moving evaporation front, and the hole depth D_r must be calculated by numerical integration. Equivalently, one can solve numerically the integral equation

$$\tau = \int_{D_0}^{D_0 + D_r} \frac{1}{\dot{D}} \, dz, \qquad (31)$$

for D_r. In Fig. 4(a) the dependence of the total drilling depth D_r on the initial position D_0 is shown. The solid line is the result of a calculation that uses Eq. (30) to express

the drilling velocity and $\alpha_{av} = 0.75$. This value for α_{av}, the only remaining free parameter in the calculation, was obtained by fitting the maximal calculated depth to the corresponding experimental value. It follows that the average temperature increase of the displaced liquid at the center of the crater is about 75% of the surface temperature rise $T_s - T_i$.

Also shown in Fig. 4(a) is the calculated drilling depth versus target position curve for pure evaporation ($\varphi = 0$), given by the dashed line. One notes that the maximum drilling depth is more than 3.5 times larger than that which would result from pure evaporation. As the target is shifted far away from the maximum drilling position, ejection ceases to be important. Only then can the experimental drilling data be explained by purely evaporative drilling.

The model overestimates the drilling depth in the wings of the curve. The parameter α_{av} affects mainly the maximum drilling depth; changing it does not improve the fit. Indeed, the width of the calculated curve in essence depends on the product $\delta^3/(\rho_l \nu \omega^2)$ [cf. Eq. (25)]. Therefore, the deviation of the calculated depths from the experimental results seems to be caused by the large uncertainty in the viscosity of molten gelatin at temperatures substantially above 100 °C and the omission of the depth dependence of the viscosity within the liquid layer. The reason why this inaccuracy does not affect the calculation more seriously is that the drilling velocity is controlled to a large extent by energy conservation at the evaporation front. Moreover, the omission of the nonlinear terms in the description of the liquid flow as well as the one-dimensional treatment of the vapor flow should be kept in mind.

The dependence of drilling velocity on position z is symmetric with respect to the beam waist position, where it attains a maximal value. On the other hand, the drilling depth versus initial target position curve cannot be symmetric because the ablation velocity rises as one drills toward the waist while it lessens, once that position is passed. Note also that the model predicts quite high temperatures in the center of the crater for the experimental conditions used, $T_s \approx 200$ °C.

B. Recoil momentum

The recoil momentum transferred to the target during ablation is often used to characterize laser-material interactions, as it is easily accessible to measurement, e.g., in a ballistic pendulum arrangement. It is usually described by the mechanical coupling coefficient C, which is defined as the ratio of the transferred momentum to the delivered pulse energy and has units of dyn s/J. For ablation of aluminum with laser pulses of a duration of 1 μs, the mechanical coupling has been shown to result from bulk target vaporization.[20]

In Fig. 4(b) the experimentally determined variation of the coupling coefficient C with the distance between the target surface and the beam waist is shown. It is very interesting to relate the experimental recoil and drilling-depth data to each other. A coarse estimate of the recoil is obtained by assuming that all the ablated material leaves the target perpendicular to its surface, the evaporated ma-

terial at a speed equal to $M_v a_v$, and the liquid ejecta at an average "ejection velocity" v_{liq}, much less than the speed of sound. The time derivative of the coupling coefficient can thus be estimated by the sum of the respective products of speed and mass removed per time as

$$\frac{dC}{dt} \approx \frac{\rho_l \pi \omega_0^2}{E_{in}} (\dot{D}_r M_v a_v + \dot{D}_m v_{liq}). \tag{32}$$

Using Eqs. (28) and (30), this is rewritten as

$$\frac{dC}{dt} \approx \frac{1}{\tau H_{lv}} \frac{M_v a_v + \varphi v_{liq}}{1 + \varphi \psi}. \tag{33}$$

For large waist-surface distances, the irradiated spot is big and ejection negligible, $\varphi = 0$. Using Eq. (33) and assuming sonic flow, the calculated coupling coefficient then becomes $C \approx a_v/H_{lv}$. At a vapor temperature T_v of 150 °C, this is much higher, $C \approx 19$ dyn s/J, than what is actually observed.[21]

The discrepancy arises because the vapor flow was modeled one dimensionally, implying a flow perpendicular to the target surface. However, molecules evaporated from different regions of the irradiated spot can interact with each other as soon as they have traveled a distance comparable to the spot diameter. As they leave the target at about the speed of sound, this happens after a very short fraction of the pulse duration used, $\tau = 200$ μs. Therefore, to accurately describe the recoil caused by the vapor, its flow must be modeled two dimensionally. Furthermore, it has been shown that the presence of the surrounding air as well as the finite surface area of the irradiated target influence the mechanical coupling coefficient.[22,23]

Still, for large-aspect-ratio holes, the gas flow is quite directional independent of pulse duration and the model here presented helps in qualitatively understanding the experimental data. Inspection of Eq. (33) shows that in that case the time derivative of the coupling coefficient decreases as the velocity ratio grows, only if $v_{liq}/(M_v a_v) < \psi$, ψ being in the range from 0.1 to 0.3 for temperatures T_s between 100 and 300 °C. This is a reasonable assumption, because the liquid slows down as it flows along the crater wall. Also, some of the displaced liquid remains in the crater, reducing the average ejection velocity v_{liq} further.

For aluminum the loss of mass of the targets has been determined simultaneously with the coupling coefficient as a function of the distance between the target surface and the beam waist. In these experiments the loss of mass was maximal, like the drilling depth, at the waist-target distance that corresponded to the minimal coupling coefficient.[2] When drilling in gelatin, the loss of mass and the drilling depth do not correlate as simply; under certain irradiation conditions a large part of the displaced liquid remains trapped inside the crater because of elastic deformations that occur during ablation.[7]

Assuming $v_{liq}/(M_v a_v) < \psi$, Eq. (33) thus implies that as ejection is enhanced, the coupling coefficient should decrease because of the reduction of the amount of evaporated mass. For the long pulse durations in mind, the influence of aspect ratio and total mass evaporated on the

target recoil can therefore be interpreted as follows: For shallow holes the vapor flows mainly parallel to the surface of the target, with but a small perpendicular velocity component. As the radial momentum components cancel each other, the coupling coefficient C becomes considerably smaller than that which would be predicted by Eq. (33). Increasing the aspect ratio raises the average velocity component of the vapor flow perpendicular to the surface of the target. Consequently, the coupling coefficient increases, as observed in Fig. 4(b) for target positions corresponding to drilling depths less than about 1 mm. Drilling deeper holes leads to smaller coupling coefficients. This is because the further increase of the hole depth reduces the total mass evaporated, but does not enhance the directionality of the vapor flow substantially. The coupling coefficient thus decreases.

The minimum in the curve shown in Fig. 4(b) is thus a consequence of minimizing the total amount of mass evaporated during the ablation process. This is equivalent, however, to maximizing the mechanical drilling. As displacing material is more efficient with respect to drilling depth than evaporating it, it becomes clear, therefore why the maximal drilling depth and the relative minimum of the coupling coefficient occur at the same target position.

V. CONCLUSION

Liquefaction of surface material prior to evaporation changes the laser-target interaction qualitatively. It enhances drilling efficiency and leads to a reduction of the evaporated mass and, consequently, of the surface temperature. These effects are important for ablation using pulses of a duration of 100 μs or longer under tight-focusing conditions. They become insignificant if the liquid cannot transverse the irradiated spot during the laser pulse, as is typically the case for Q-switched pulses.

A steady-state model is developed that describes ablation as a combination of evaporation and ejection. Using energy balance and linearized Navier–Stokes equations for a boundary layer, an upper limiting value for the drilling velocity is obtained. The drilling velocity is found, as a rule, to increase with increasing depth of energy deposition, decreasing liquid viscosity, and smaller spot size.

The recoil momentum induced on the target depends predominantly on the vapor-flow pattern. This becomes more and more directional as the aspect ratio of the drilled holes increases. In that case the coupling coefficient is dominated by the total amount of evaporated mass.

[1] M. Frenz, V. Romano, A. D. Zweig, H. P. Weber, N. I. Chapliev, and A. V. Silenok, J. Appl. Phys. 66, 4496 (1989).

[2] M. Bass, M. A. Nassar, and R. T. Swimm, J. Appl. Phys. 61, 1137 (1987).

[3] V. A. Batanov and V. B. Fedorov, JETP Lett. 17, 247 (1973).

[4] M. von Allmen, J. Appl. Phys. 47, 5460 (1976).

[5] C. L. Chan and J. Mazumder, J. Appl. Phys. 62, 4579 (1987).

[6] A. D. Zweig and H. P.Weber, IEEE J. Quantum Electron. QE-23, 1787 (1987).

[7] A. D. Zweig, M. Frenz, V. Romano, and H. P. Weber, Appl. Phys. B 47, 259 (1988).

[8] C. J. Knight, AIAA J. 17, 519 (1979).

[9] Y. V. Afanas'ev and O. N. Krokhin, Sov. Phys. JETP 25, 639 (1967).

[10] J. F. Ready, Effects of High Power Laser Radiation (Academic, Orlando, FL, 1971), pp. 95–115.

[11] O. N. Krokhin, in Laser Handbook, edited by F. R. Arrecchi and E. O. Schulz-Du-Bois (North-Holland, Amsterdam, 1972), pp. 1371–1407.

[12] The mean free path of molecules in air at ambient conditions is about 65 nm and much less for water vapor at high pressures [R. C. Weast, CRC Handbook of Chemistry and Physics (CRC, Boca Raton, FL, 1985), p. F148].

[13] R. C. Weast, CRC Handbook of Chemistry and Physics (CRC, Boca Raton, FL, 1985), p. D181.

[14] R. C. Weast, CRC Handbook of Chemistry and Physics (CRC, Boca Raton, FL, 1985), pp. E16–E23.

[15] V. M. Zolotarev, B. A. Mikhailov, L. I. Alperovich, and S. I. Popov, Opt. Spectrosc. 26, 430 (1969).

[16] J. Frauchiger and W. Lüthy, Opt. Quantum Electron. 19, 231 (1987).

[17] It should read $\eta_0(dv/dz)r\Delta r\Delta\varphi$ instead. As in Ref. 6, the viscosity of the liquid was assumed to equal the value for 60 °C, the mistake was numerically compensated, and not noticed from the comparison with the experimental data. As a consequence, Eqs. (12)–(17) in Ref. 6 as well as Eqs. (5) and (8) in Ref. 7 are wrong by the same factor δ/ω_0.

[18] F. V. Bunkin and M. I. Tribel'skiĭ, Sov. Phys. Usp. 23, 105 (1980).

[19] J. T. Walsh, Jr. and T. F. Deutsch, Lasers Surg. Med. 9, 327 (1989).

[20] D. I. Rosen, J. Mitteldorf, G. Kothandaraman, A. N. Pirri, and E. R. Pugh, J. Appl. Phys. 53, 3190 (1982).

[21] Taking into account the back pressure of the outside atmosphere reduces the calculated coupling coefficient by $-p_{ext}/I \approx -1$ dyn s/J.

[22] A. N. Pirri, Phys. Fluids 16, 1435 (1973).

[23] J. P. Reilly, A. Ballantyne, and J. A. Woodroffe, AIAA J. 17, 1098 (1979).

1691   J. Appl. Phys., Vol. 70, No. 3, 1 August 1991

A. D. Zweig   1691

P-4

Infrared Tissue Ablation:
Consequences of Liquefaction

A.D. Zweig

Wellman Laboratories of Photomedicine
Massachusetts General Hospital
Boston, MA 02114

Abstract

Ablation of biological targets by highly-absorbed infrared laser pulses (duration 200 μs) is explained using a model that takes into account tissue liquefaction. The generation of a liquid layer in tissue leads to an enhancement of the drilling efficiency and to a reduction of the evaporation rate. Experimental drilling-depth and recoil-momentum data are explained by a combination of evaporation and ejection.

1 Introduction

In modern surgery CO_2 lasers are being used routinely to perform high precision cutting of tissue. Today the Er:YAG laser, which emits at the infrared absorption peak of water, allows, in principle, an even higher cutting precision. However, with the application of pulsed lasers in surgery there has been a growing awareness that tissue ablation is an "explosive event" rather than a straightforward evaporative process [1].

There has been no direct experimental evidence for the existence of a liquid zone during ablation. This is primarily because it is thin, of the order of the optical penetration depth of the laser radiation, and hidden inside the drilled crater. However, indirect confirmation of the liquid layer is provided by some experimental findings obtained using laser pulses longer than 100 μs under tight-focusing conditions, i.e. spot diameters of less than half a mm. Of particular practical importance are the extension and repetition-rate dependence of lateral thermal damage along CO_2 laser incisions as well as the axial transport of biologically active material into laser craters [2] [3] [4].

Here I intend to further solidify the concept of "liquefied tissue" by connecting recent drilling-depth and recoil-momentum measurements on tissue and gelatin targets. After a description of the generation of the liquid layer I proceed to explain how ablation can be understood as a combination of evaporation and liquid ejection. This concept is then applied to drilling depth and recoil momentum.

2 Liquid Layer

As a target absorbs intense radiation, a surface layer is heated and begins to evaporate. Even before evaporation that layer undergoes structural changes. Its thickness depends on the depth of energy deposition. For infrared-laser tissue ablation the thickness is usually determined by absorption of radiation rather than heat conduction.

Suppose that the thickness of the liquid layer was determined predominatly by heat conduction. The distance, δ_c, over which conduction acts is $\sqrt{\kappa t_c}$, where $\kappa \approx 1.22 \cdot 10^{-3}$ cm^2/s is the thermal diffusivity for excised animal dermis [5]. After the onset of drilling, the time, t_c, during which conduction acts is given by the time it takes to ablate a layer of thickness, δ_c, rather than simply the laser pulse duration. In that case t_c becomes equal to the layer thickness, δ_c, divided by the drilling velocity, $\dot{D}$. The layer thickness caused by heat conduction alone thus amounts to $\delta_c = \kappa/\dot{D}$, which is already equal to the minimal optical penetration depth in the infrared, $d = 0.75$ μm at 2.94 μm wavelength [6] [7], at a drilling velocity of 0.16 m/s. For larger drilling velocities, therefore, the extension of the liquid layer is dominated by the radiation absorption.

The extension of the liquid layer can be calculated by applying energy balance to an infinitesimal volume element at a fixed distance away from the surface of the liquid layer. Assuming a temperature of the liquid of 150 °C one finds that the thickness of the liquid
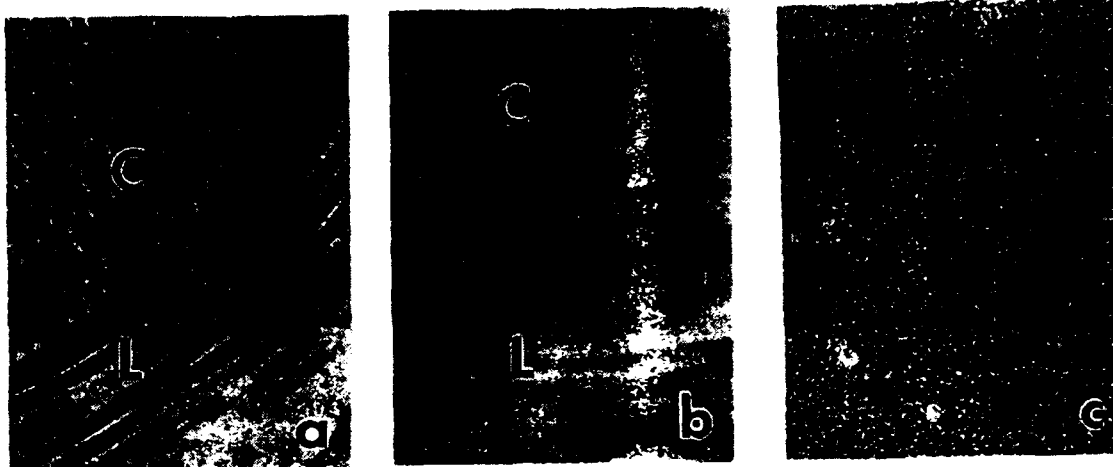
Figure 1: Photomicrograph showing the ultrastructure of collagen fibrils in the corium of (ICR) mice in cross (C) and longitudinal (L) section. Freshly excised skin samples were thermally altered by immersion in a heat bath of temperature T_b for 160 seconds. (a): $T_b = 53$ °C: The fibrils are normal. (b): $T_b = 65$ °C: The fibrils are thickened to about twice the normal size. (c) $T_b = 80$ °C: The collagen fibres are completely dissolved. ×31,000 (from [3])

layer generated during ablation is about 1.5 times the optical penetration depth.

Water and gelatin melt at well defined temperatures which can easily be measured. It is less obvious how a liquid layer is generated in tissue, which does not undergo an equally clear-cut phase transition. Tissue can be regarded as "liquefied", however, as soon as its shear strength is overcome by shear forces. Then adjacent layers of tissue move relative to each other, much as in any viscous flow. For intact skin this occurs at pressures comparable to its tensile strength, $\sim$ 100 bar [8]. Such high ablation pressures are not generated at irradiances of less than ~ 1 MW/cm^2.

Thermally damaged tissue is expected to flow at much lower pressures, as the associated structural changes weaken the tensile strength considerably. In skin, for example, where collagen fibers are responsible for the high tensile strength, this assumption is supported by an observation of their thermally-induced decay. In Fig. 1 the ultrastructure of collagen fibrils harvested from thermally altered mice skin (corium) is shown. The skin samples were thermally damaged by immersion in a heat bath of a constant temperature for 160 seconds. Fig. 1 shows how the collagen fibrils dissolve, and therefore weaken, with increasing temperature, T_b, of the heat bath. Long (160 seconds) exposure at 80 °C destroys the collagen structure completely. Similar changes are expected for short thermal exposures, provided that the tem-

peratures are high enough.

In summary, during ablation there is a surface layer that has a reduced tensile strength and flows more easily under the action of shear forces than the bulk of the target. Its thickness is of the order of the optical penetration depth.

3 Ablation Model

Theoretical models of ablation tend to become elaborate when pushed to increasing rigorousness. I will describe the ablation process qualitatively, stressing the principles involved rather than their mathematical description. A more detailed presentation of similar ideas can be found in the literature [9].

Vaporization of materials by intense laser radiation has been modelled by many. Early works treat vaporization into vacuum [10] [11], while a more recent one also considers the influence of a non-vanishing back pressure [12]. One main conclusion of these works is that the surface temperature increases monotonically but weakly with the incident irradiance. This is found, in principle, by combining a Clausius-Clapeiron equation for saturated vapor temperature and pressure with the fact that the vapor pressure depends linearly on the amount of evaporated material (cf. also [13]).

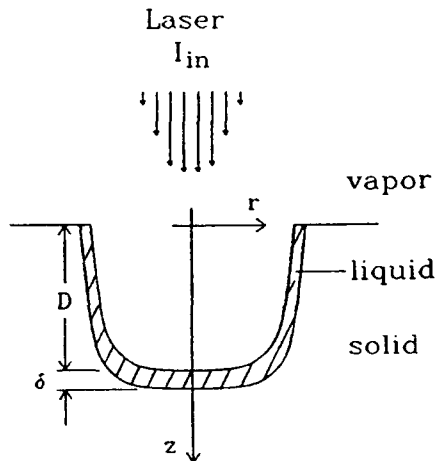The pressure that pushes on the surface from which

Figure 2: Schematic diagram illustrating the model. At the bottom of the crater, which has a depth, $D(t)$, a liquid layer of thickness, δ, forms between vapor and solid. Material is pushed outwards, enhancing drilling. At the center of the crater the flow is to a good approximation radial.

evaporation proceeds is determined by momentum conservation. It increases with irradiance and is about equal to 55% of the vapor pressure for sonic flow [14]. The induced ablation pressures will therefore change spatially with the variation of irradiance on the target. This induces shear forces inside the liquid surface layer. Thus for a Gaussian beam, where the intensity drops from the center to the edge, liquid flows radially towards the periphery (cf. Fig. 2). Other beam profiles may cause a more complicated flow structure within the liquid layer. However, some liquid will always be pushed towards the crater wall. At the wall the liquid changes direction and flows axially out of the hole. How much of this displaced material actually leaves the crater depends on its flow properties as well as on the shape of the crater wall during ablation. Such questions are important with respect to the thermal damage remaining after ablation, but will not be addressed here.

To quantify the enhancement of drilling by this mechanical ejection mechanism, one needs to study the hydrodynamics of the induced flow. Here I shall take, for simplicity, a rather phenomenological point of view and assume that ejection is present, and that its effect is determined from experiment. The drilling velocity, $\dot{D}$, thus becomes a sum of two terms, the thermal drilling velocity caused by evaporation, $\dot{D}_t$, and the mechanical contribution, $\dot{D}_m$. The strength of the mechanical drilling component is conveniently

measured in terms of the *corresponding* evaporative contribution. Therefore I define the ratio of the two drilling velocities (at the center of the crater) as

$$\varphi = \dot{D}_m / \dot{D}_t \qquad (1)$$

φ depends on the irradiation parameters as well as on the hydrodynamic properties of the target material. Note that φ does *not* directly give the amplification of the drilling velocity due to the presence of the liquid layer, but rather the relative strength of the two contributions, under the assumption that they are *both* present. φ increases as it becomes easier to move liquid in the radial direction. Therefore, for given irradiance, φ grows with increasing thickness and decreasing viscosity of the liquid layer, as well as with decreasing spot size of the drilling beam. This is only true for sufficiently long pulses. Otherwise the liquid moves less than a spot radius, ω_0, during the pulse duration, and the mechanical contribution, $\dot{D}_m$, becomes negligible. This will be the case for Q-switched pulses with a duration of $\tau \approx 10$ ns. Taking the sound speed in water, $a = 1.5$ km/s, as an upper limit for the flow velocity, the product, $\tau a \approx 15$ μm, is smaller than most spot sizes realized in ablation experiments.

A good qualitative understanding of the ablation process can be gained from an energy balance at the surface of the irradiated target. I assume steady state drilling has been established. The incident irradiation, I_{in}, is then split between the two energy-consuming processes, evaporation and ejection.

$$I_{in} = \rho_l H_{lv} \dot{D}_t + \rho_l c_l (T_l - T_i) \dot{D}_m \qquad (2)$$

Here ρ_l, c_l and T_l denote the density, the specific heat and the temperature of the liquid. I shall use thermal properties of water, i.e. $\rho_l = 1$ g/cm^3, $c_l = 4.2$ J/(g $\cdot$ K) and an initial temperature of $T_i = 20$ °C. H_{lv} is the enthalpy difference between the target material at the initial temperature, T_i, and the evaporated target material. H_{lv} depends only weakly on the temperature of the vapor; $H_{lv} = 2.73 \pm 0.1$ kJ/g in the temperature range from 100 °C to the critical temperature, $T_c = 374$ °C.

Using Eqs. (1-2) the total drilling velocity $\dot{D} = \dot{D}_t + \dot{D}_m$ can be written as

$$\dot{D} = \frac{I_{in}}{\rho_l} \frac{1 + \varphi}{H_{lv} + \varphi c_l (T_l - T_i)} \qquad (3)$$

According to equation (3) the drilling velocity increases steadily with the contribution of ejection. $\varphi = 0$ characterizes the purely evaporative process, while $\varphi = \infty$ gives the upper limit on the drilling
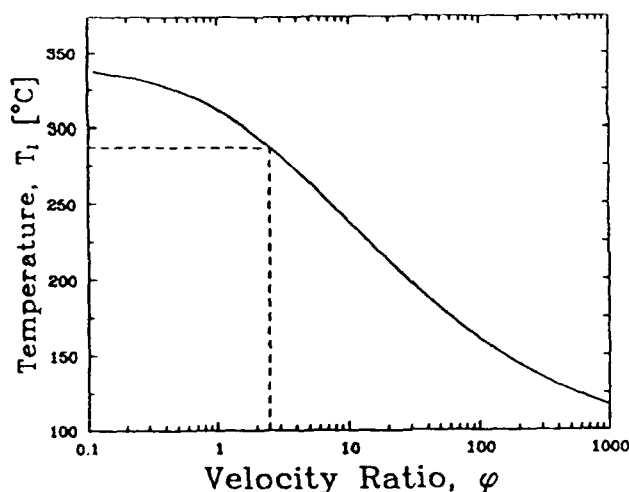
Figure 3: Calculated liquid temperature, T_l, versus $\varphi = \dot{D}_m/\dot{D}_t$, the ratio between the mechanical drilling velocity, $\dot{D}_m$, and the evaporative contribution, $\dot{D}_t$, for an incident irradiance of 2.5 MW/cm^2. The temperature, T_l, is determined predominantly by the evaporation rate. Therefore it drops with increasing φ, as more and more energy is used to heat up liquid displaced during the ablation. At $\varphi = 2.5$ (dashed line), the two drilling processes consume equal amounts of energy.

velocity, when the energy spent on evaporation can be neglected. If φ, the ratio between mechanical and thermal drilling velocity, increases, less energy is available for evaporation. The evaporation rate is thus reduced; this lowers the liquid temperature, T_l. This is illustrated in Fig. 3. There the liquid temperature, T_l, is plotted versus φ. The calculation assumed a target irradiance of 2.5 MW/cm^2. For a small mechanical contribution the energy is mainly used to evaporate material, while otherwise a significant amount of energy is spent to heat up the liquid displaced during ablation. The breakeven point, determined from Fig. 3 and eq. (2), is found at $\varphi = 2.5$.

4 Discussion

In this section the model will be used to explain drilling depth and recoil measurements. Both are quite easily accessible to experimental investigation and yield important information on the drilling mechanism. Published measurements, obtained from ablation of tissue and gelatin targets with single Er:YAG laser pulses will be discussed [15]. In these experiments a TEM$_{00}$-beam with a beam waist of $\omega_0 = 72$ μm and a peak irradiance of 2.5 MW/cm^2 was

used. The laser pulses had a duration of $\tau = 200$ μs and a pulse energy of $E_{in} = 40$ mJ. These parameter values will be assumed in the following.

4.1 Drilling depth

Under tight-focusing conditions it is quite common to drill to depths comparable to or larger than the confocal distance, $z_0 = \pi\omega_0^2/\lambda$. Then the irradiance at the phase boundary, and therefore also the drilling velocity, change significantly during drilling. As a consequence the total drilling depth is not just a product of the pulse duration and the initial surface recession speed, but has to be calculated, instead, by numerical integration using the drilling velocity.

The drilling depth becomes maximal if the beam waist is located exactly halfway down the drilled crater. A little thought shows that this holds because of the monotonic increase of the drilling velocity with irradiance. In Fig. 4 the calculated maximal drilling depth is plotted versus the ratio, φ, of the two material removing processes assuming the laser parameters given above. The dashed lines indicate the maximal depths in skin and gelatin, determined from experimental data plotted in Fig. 5a, as well as the corresponding average values of φ. This calculation is approximate, as it assumes φ is constant, while in reality φ depends on irradiance as well as on the details of the flow and changes during the ablation. Still the calculation illustrates the consequence of the ejection mechanism on the maximal drilling depth.

In Fig. 5a the drilling depth measured in tissue and in gelatin containing 80% water is displayed as a function of the distance between the beam waist and the target surface at the beginning of the laser pulse. The short-dashed line indicates the (calculated) depth for purely evaporative drilling into a water target. As is made clear by the figure, the experimental values are too large to be caused by evaporation only. The enhanced drilling depth originates from the ejection mechanism.

4.2 Recoil momentum

The recoil momentum, caused by the ejected material during an ablation process on a target, provides another simple means of characterizing the interaction, as it can be measured quite easily in a ballistic pendulum arrangement. The total recoil momentum divided by the pulse energy is called the mechanical coupling coefficient, C, and has units of dyn·s/J. In Fig. 5b its dependence on the beam waist to tar-
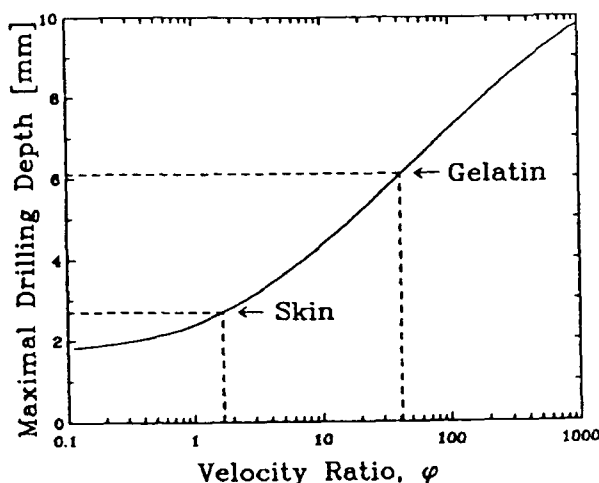
Waist—Surface Distance [mm]

Figure 4: Calculated maximal drilling depth versus $\varphi = \dot{D}_m/\dot{D}_t$, the ratio between the mechanical drilling velocity, $\dot{D}_m$, and the evaporative contribution, $\dot{D}_t$, for an incident irradiance of 2.5 MW/cm². Depths were calculated by numerical integration of drilling velocity assuming the beam waist to be halfway down the laser crater. The dashed lines indicate the experimentally determined maximal depths in skin and gelatin containing 0.84 g/cm³ water and the corresponding average φ values (cf. Fig. 5a).

get distance is shown. The similar appearance of the curves for gelatin and skin indicates that the laser-target interaction is qualitatively identical for the two media.

To roughly estimate the total recoil momentum caused by the ablation process, I assume that ejection contributes little. Indeed this seems to be a reasonable assumption, as the liquid is slowed down during its flow along the crater walls. It will therefore leave the target at a much lower speed than the vapor. Furthermore, not all of the displaced liquid is actually ejected during the ablation.

Therefore, neglecting the contribution of liquid ejecta, the recoil momentum is estimated by assuming that all the evaporated material leaves the target at the speed of sound, a_v. Correspondingly the coupling coefficient, C, becomes

$$C \approx (\rho_l \pi \omega^2 \tau \dot{D}_t) a_v / E_{in} \qquad (4)$$

Using Eqs. (1,3) this is rewritten as

$$C_{ev} \approx \frac{a_v}{H_{lv} + \varphi c_l(T_l - T_i)} \qquad (5)$$

For large spot sizes, where there is no ejection, e.g. $\varphi = 0$, the calculated coupling coefficient becomes
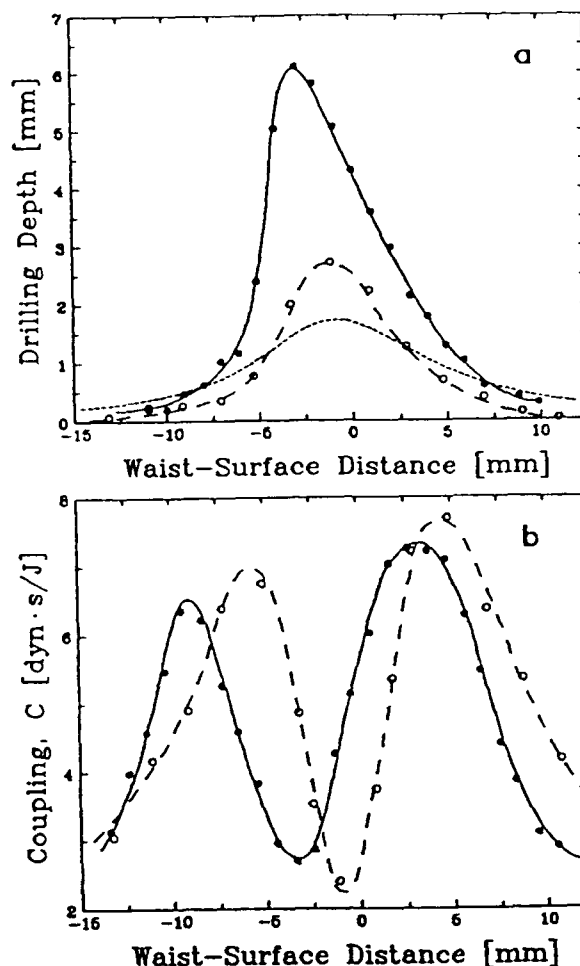
Waist—Surface Distance [mm]

Figure 5: Influence of the initial position of the target surface on the drilling mechanism. Positive (negative) positions correspond to a beam waist located outside (inside) the target. Experimental data is indicated by open circles (o) for skin targets and by filled circles (•) for gelatin containing 0.84 g/cm³ water. All the holes were drilled with single laser pulses ($\lambda = 2.94$ μm, $\tau = 200$ μs, $\omega_0 = 72$ μm, $E_{in} = 40$ mJ). Data from [15]. The lines are intended to guide the eye. (a): Drilling depth versus waist-target distance. For comparison the drilling depth in case of pure evaporation, calculated by numerical integration, is shown as a short-dashed line. (b): Coupling coefficient, C, versus waist-target distance. C is equal to the total recoil momentum normalized by the laser pulse energy. Note that C has a relative minimum when the drilling depth has a maximum.

$C \approx a_v/H_{lv}$. At a vapor temperature of $T_v = 150$ °C this is much higher, $C \approx 19$ dyn · s/J, than what is actually observed, ≤ 3 dyn · s/J [1].

---
[1] Taking into account the back pressure of the outside at-

The discrepancy arises because the vapor flow was modelled one-dimensionally, implying a flow perpendicular to the target surface. However, molecules evaporated from different regions of the irradiated spot can interact with each other as soon as they have travelled a distance comparable to the spot diameter. As they leave the target at about the speed of sound, this happens already after a very short fraction of the pulse durations used, $\tau = 200 \; \mu s$. Therefore, to accurately describe the recoil caused by the vapor, its flow must be modelled two-dimensionally [16]. Nevertheless, for large aspect-ratio holes the gas flow is quite directional independent of pulse duration. Then the model here presented helps in qualitatively understanding the experimental data. It predicts that the total amount of mass evaporated determines the recoil momentum.

The recoil curves can be interpreted by the influence of aspect ratio and total mass evaporated: For shallow holes the vapor flows mainly parallel to the target surface, with only a small velocity component perpendicular to the surface of the target. As the radial momentum components cancel each other because of symmetry, the coupling coefficient, C, thus becomes considerably smaller than the prediction based on the eq. (5). Increasing the aspect ratio raises the perpendicular velocity component of the vapor flow, and therefore also the coupling coefficient. This rise is seen in Fig. 5b for target positions corresponding to drilling depths smaller than about a mm. For larger drilling depths the coupling coefficient is seen to decrease with increasing depths. This is because the further increase of the hole depth does not enhance the directionality of the vapor flow substantially, but it reduces the total mass evaporated. The coupling coefficient thus decreases, as predicted by eq. (5) due to the larger average φ value associated with the enhanced mechanical contribution to drilling.

The minima in the curves shown in Fig. 5b are thus a consequence of minimizing the total amount of mass evaporated during the ablation process. This is equivalent, however, to maximizing the ejection mechanism. As ejection is more efficient than evaporation with respect to drilling depth, it becomes clear, therefore, why the maximal drilling depth and the relative minimum of the coupling coefficient in Fig. 5 occur at the same target position.

5 Conclusion

Liquefaction of the target surface prior to evaporation changes the laser-target interaction qualitatively. The associated effects are important for ablation of tissue by pulses of a duration of 100 μs or longer under tight-focusing conditions. They become insignificant if the liquid cannot transverse the radius of the irradiated spot during the laser pulse, as is typically the case for Q-switched pulses.

Drilling depth and recoil momentum caused by pulsed laser ablation change with distance of the target surface from the beam waist position in a characteristic way, qualitatively identical for tissue and gelatin targets. The experimental findings are explained by a model that describes ablation as a combination of evaporation and ejection.

The generation of a liquid layer at the phase boundary and its radial displacement during ablation lead to an increase of the drilling efficiency. The associated reduction of the evaporation rate causes a reduction of the temperature at the target surface during ablation.

The recoil momentum induced on the target depends predominantly on the vapor flow pattern. This becomes more and more directional as the aspect ratio of the drilled holes increases. In that case the coupling coefficient is dominated by the total amount of evaporated mass.

6 Acknowledgments

References

[1] J.T. Walsh, Jr. and T.F. Deutsch. "Effect of tissue mechanical properties on pulsed CO_2 laser ablation rates". *IEEE Trans. on Biomed. Eng.*, 36:1195–1201, 1989.

[2] V. Venugopalan, N.S. Nishioka, and B.B. Mikić. "The effect of CO_2 laser pulse repetition rate on tissue ablation rate and thermal damage". *IEEE Trans. on Biomed. Eng.*, to appear.

---

mosphere does not help enough, as the associated reduction of the coupling coefficient, $-p_{est}/I \approx -1$ dyn $\cdot$ s/J, is too small.

[3] A.D. Zweig, B. Meierhofer, O.M. Müller, C. Mischler, V. Romano, M. Frenz, and H.P. Weber. "Lateral thermal damage along pulsed laser incisions". *Lasers Surg. Med.*, 10:262–274, 1990.

[4] M. Frenz, F. Mathezloic, M.H.S. Stoffel, A.D. Zweig, V. Romano, and H.P. Weber. "Transport of biologically active material in laser cutting". *Lasers Surg. Med.*, 8:562–566, 1988.

[5] H.F. Bowman and E.G. Cravalho. "Theory, measurement, and application of thermal properties of biomaterials". *Ann. Rev. Phys. Bioeng.*, 4:43–80, 1975.

[6] V.M. Zolotarev, B.A. Mikhailov, L.I. Alperovich, and S.I. Popov. "Dispersion and absorption of liquid water in the infrared and radio regions of the spectrum". *Opt. Spectroscopy*, 26(1):430–432, 1969.

[7] J. Frauchiger and W. Lüthy. "Interaction of 3 μm radiation with matter". *Opt. Quantum Electron.*, 19:231–235, 1987.

[8] H.G. Vogel. "Collagen and mechanical strength in various organs of rats treated with d-penicillamine or amino-acetonitrile". *Connective Tissue Research*, 3:237–244, 1975.

[9] C.L. Chan and J. Mazumder. "One-dimensional steady-state model for damage by vaporization and liquid expulsion due to laser-material interaction". *J. Appl. Phys.*, 62(11):4579–4586, 1987.

[10] Y.V. Afanas'ev and O.N. Krokhin. "Vaporization of matter exposed to laser emission". *Sov. Phys. JETP*, 25(4):639–645, 1967.

[11] O.N. Krokhin. "Generation of high-temperature vapors and plasmas by laser radiation". In F.T. Arrecchi and E.O. Schulz-Du-Bois, editors, *Laser Handbook*, pages 1371–1407, North-Holland, Amsterdam, 1972.

[12] C.J. Knight. "Theoretical modeling of rapid surface vaporization with back pressure". *AIAA*, 17(5):519–523, 1979.

[13] J.F. Ready. *Effects of high power laser radiation*, pages 95–115. Academic Press, Inc., Orlando, Florida, 1971.

[14] C.J. Knight. "Transient vaporization from a surface into vacum". *AIAA*, 20(7):950–954, 1982.

[15] M. Frenz, V. Romano, A.D. Zweig, H.P. Weber, N.I. Chapliev, and A.V. Silenok. "Instabilities in laser cutting of soft media". *J. Appl. Phys.*, 66(9):4496–4503, 1989.

[16] A.N. Pirri. "Theory for momentum transfer to a surface with a high-power laser". *Physics of Fluids*, 16(9):1435–1440, 1973.

Photons and Low Energy Particles in Surface Processing

Symposium held December 3-6, 1991, Boston, Massachusetts, U.S.A.

EDITORS:

Carol I.H. Ashby
Sandia National Laboratories, Albuquerque, New Mexico, U.S.A.

James H. Brannon
IBM Almaden Research Center, San Jose, California, U.S.A.

Stella W. Pang
University of Michigan, Ann Arbor, Michigan, U.S.A.

47

GENERATION OF SHOCK WAVES IN CONFINED EXCIMER LASER ABLATION OF POLYIMIDE

ADRIAN D. ZWEIG AND T.F. DEUTSCH
Wellman Laboratories of Photomedicine, Massachusetts General Hospital, Boston, MA 02114

ABSTRACT

We study acoustic effects associated with the ablation of polyimide under water confinement. Ablation launches a shock in the targ t. After the shock propagates into the surrounding water we measure its velocity with an optical probe system. In the water the shocks decay after propagating a few hundred microns. The peak shock pressure scales with the square root of the laser f ence. Our observations can be explained by a simple model tha terprets the generated pressures as being due to the heating a a confined ideal gas.

INTRODUCTION

A shock wave differs qualitatively from an acoustic pressure transient. It is characterized by a supersonic propagation speed and a very steep front that for all practical purposes can be treated as a discontinuity in pressure, density, particle velocity and internal energy. At a shock front the pressure rises a few kbars within a distance of some nanometers, resulting in pressure transients with risetimes of only a few picoseconds [1]. A shock also changes the thermodynamic state of the medium in which it propagates in a different way than an adiabatic process does.

During shock propagation all the energy dissipation occurs within the shock front, which is very thin. Because of this, shock waves are unique, very intense sources of energy that are possibly relevant for causing photoacoustic damage to cells, macromolecules and tissue. The aim of this study was to investigate the conditions under which shocks are generated by excimer-laser ablation of polymers and biological tissues. To date, only acoustic pressure transients of several hundred bars with risetimes of a few nanoseconds have been measured (2,3).

In order to study the acoustic effects associated with UV-laser ablation we investigated the ablation of a thin (25 µm) sheet of polyimide immersed in distilled water. Using an optical probe system we measure the velocities of the laser-induced stress waves in the water as a function of incident laser fluence. The measured supersonic velocities indicate the formation of shock waves. Because the equation of state of water is known, the corresponding peak pressures follow directly from the jump conditions at the shock front.

Our observations are explained by a simple ideal-gas model. We show that shocks are generated by the expansion of the hot gaseous ablation products.

MATERIALS AND METHODS

The setup is illustrated in Fig. 1. For ablation we use a XeCl excimer laser (Lambda Physik model EMG 103 MSC) emitting pulses of a duration of 20 ns at 308 nm wavelength. To select an uniform part of the laser beam we place a 5-mm aperture in its path. The beam is attenuated by filters and focused by an aspheric lens with a focal length of 18 mm into a cuvette that is filled with distilled water. As targets we use sheet polyimide of a thickness of 25 μm immersed in water.

To determine the velocity of shock waves propagating in water we use an optical probe technique that was described in detail elsewhere [4]. We focus two TEM_{00} Helium-Neon probe beams into our cuvette in such a way that they are parallel to each other and to the surface of the target. X-z-translation stages allow us to displace the probe beams parallel and perpendicular to the surface of the target without changing their separation, which is about 15 μm.

The transient changes in the index of refraction that are caused by the pressure waves in the water temporarily deflect the probe beams out of the acceptance angle of the detection optics. We monitor this with a fast photodiode (D2) (EG&G, FND 100, risetime < 1 ns). The resulting signal is digitized by a Tektronix digitizer (model AD 7912, 750-MHz bandwidth), transferred to an IBM-AT-clone computer on a GPIB bus and analyzed with a computer program. In this way we determine the transit time of a pressure wave through the axes of our two probe beams to an accuracy of 0.5 ns. At sufficiently large distances from the target, the pressure waves become sonic and propagate at the velocity of sound in water. This allows us to determine the distance between the two probe beams from a measurement of the transit time far away from the target.

An average fluence F of the ablating pulse at the target surface is calculated from pulse energy and spot size. We determine the energy of the ablating pulse by measuring a split-off part of the beam with a pyroelectric detector (D1) (Molectron model J3-09). To vary the pulse energy during the experiment we reduce the maximum pulse energy of about 4 mJ by attenuating filters (F). The spot size is determined by microscopic examination of the irradiated region. The observed burn pattern is elliptical with an area $A=4.4 \cdot 10^{-5}$ cm^2.
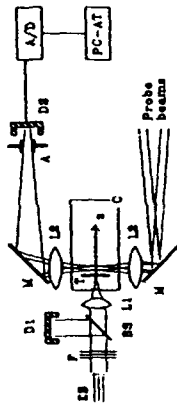

Figure 1: Schematic view of the experimental setup. The z-axis is the axis of the excimer beam EB with z=0 at the rear surface of the target. C cuvette filled with water, T target, BS beam splitter, M mirror, Li lenses, Di detectors, F neutral density filter, A aperture, A/D digitizer.

RESULTS

At a fluence of $F_0=50$ mJ/cm^2, about equal to the threshold of ablation determined in air by photoacoustic techniques (45 mJ/cm^2 [5,6]), we begin detecting pressure waves that propagate at a speed about 5 % or 75 m/s above the speed of sound from the irradiated surface of the target towards the focusing lens. The corresponding pressure transients near the back side of the target are too small to be detected by our probe system.

For fluences between 130 mJ/cm^2 and about 100 J/cm^2 we monitor the strength of the shock waves that are launched in the polyimide by measuring their velocities after propagation into the water at the back side of the target. During spherical expansion in the water, these velocities drop to the speed of sound within a distance of a few hundred microns.

The peak pressure of a shock wave is related to the shock velocity U_s and to the particle velocity u_p by the jump condition

$$P_s = \varrho_0 U_s u_p, \qquad (1)$$

where P_s is the shock pressure and $\varrho_0=0.987$ g/cm^3 the density of water at 20 °C. U_s and u_p are further related by the equation of state. To first approximation

$$U_s = a + b u_p, \qquad (2)$$

with the values a=1.483 km/s and b=2.07 for water [7]. Using (1) and (2) we calculate the shock pressures P_s from shock velocities U_s that are measured during the supersonic propagation of the shocks in the water.

Shock pressures determined from the measured shock velocities are presented in Fig. 2a-b. Fig. 2a shows the dependence of the shock pressure $P_s(z_0,F)$ on the fluence F of the ablating pulse at the fixed distance $z_0=25$ μm away from the rear surface of the target. The pressures were calculated from shock velocities U_s measured at z_0. In a double-logarithmic plot the pressures are well fitted by a straight line (dashed) with a slope of 0.52. The two solid lines in Fig. 2a are theoretical predictions from the ideal-gas model discussed below. They were calculated by assuming the gas to have a molar specific heat at constant volume of either $c_v=5/2$ R or $c_v=6$ R, R being the universal gas constant.

In Fig. 2b we show the decay of the shock pressure with distance z from the rear surface of the target at z=0. These pressures were calculated from velocities measured at distance z for the two fluences $F_1=16.5$ J/cm^2 and $F_2=0.7$ J/cm^2. At large enough distances z the shock waves expand spherically, and, because of momentum conservation, their pressure P_s then varies inversely with the square of the distance from the center of the shock [4]. Accordingly we fit the data by

$$P_s(z,F_i) = P_i [(z_0-z_i)/(z-z_i)]^2, \qquad (3)$$

CONCLUSION

The shock waves generated by ablation of polyimide confined in water using 308-nm excimer-laser radiation have been studied. The measured shock pressures are proportional to the square root of the fluence of the ablating pulse. This can be explained by a simple thermal model that describes the expansion of a confined ideal gas subjected to rapid heating.

According to the model, the ablation pressure depends on irradiance, on the specific heat of the gas mixture created during the ablation and on the acoustic impedances of the target and the confining material. Qualitatively this remains true for a film supported in air or vacuum. In these cases however, because of different gas expansions, lower pressures than those reported here and other functional dependences on the incident fluence are expected.

ACKNOWLEDGEMENTS

REFERENCES

[1] P. Harris and H.N. Presles, J. Chem. Phys. $\underline{77}$, 5157 (1982)

[2] P.E. Dyer and R. Srinivasan, Appl. Phys. Lett. $\underline{48}$, 445 (1986)

[3] F.W. Cross, R.K. Al-Dhahir and P.E. Dyer, J. Appl. Phys. $\underline{64}$, 2194 (1988)

[4] A.G. Doukas, A.D. Zweig, J.K. Frisoli, R. Birngruber and T.F. Deutsch, Appl. Phys. B $\underline{53}$ (1991), in press

[5] R.S. Taylor, D.L. Singleton and G. Paraskevopoulos, Appl. Phys. Lett. $\underline{50}$, 1779 (1987)

[6] P.E. Dyer and J. Sidhu, J. Appl. Phys. $\underline{57}$, 1420 (1985)

[7] P. Harris and H.N. Presles, J. Chem. Phys. $\underline{74}$, 6864 (1981)

[8] R.D. Griffin, B.L. Justus, A.J. Campillo and L.S. Goldberg, J. Appl. Phys. $\underline{59}$, 1968 (1986)

[9] R. Fabbro, J. Fournier, P. Ballard, D. Devaux and J. Virmont, J. Appl. Phys. $\underline{68}$, 775 (1990)

[10] G. Herzberg, Molecular spectra and molecular structure, II. Infrared and Raman spectra of polyatomic molecules, (D. van Nostrand Co., Princeton NJ, 1968) pp. 501-519.

[11] J.H. Brannon, J.R. Lankard, A.I. Baise, F. Burns and J. Kaufmann, J. Appl. Phys. $\underline{58}$, 2036 (1985)

[12] R. Srinivasan, B. Braren and R.W. Dreyfus, J. Appl. Phys. $\underline{61}$ (1987)

sure wave) while the lower trace displays the Ho:YAG pulse waveform. The first pressure pulse corresponds to the peak of the laser pulse and is believed to result from the mechanism of optical sound generation.[1] The second and higher-magnitude pressure pulse occurs at the end of the Ho:YAG laser pulse, coinciding with the timing for bubble collapse (Fig. 1) which is believed to be the source for this pressure wave. The subsequent pressure signals may be caused by the ringing of the transducer or by echoes, and needs further clarification.

Generation of cavitation bubbles and the associated pressure transients may be important mechanisms for the tissue tearing and dissection observed from previously reported mid-infrared laser soft tissue ablation studies.[2] In addition, the strong interaction between mid-infrared laser pulses with fluid and the induced pressure wave should be carefully monitored in ophthalmic use of these lasers. Understanding and control of there res-
vel-
ical

pp.

in
tro-
gest
ica,
2

3:15 pm

CThL4 Shock waves generated by XeCl excimer laser ablation of polyimide in air and water

A. D. Zweig, T. F. Deutsch, *Wellman Laboratories of Photomedicine, Massachusetts General Hospital, Boston, MA 02114*

Pressure transients of several hundred bars with rise times of a few nanoseconds can be created by UV-laser ablation of organic polymers as well as of tissue.[1,2] We demonstrate, we believe for the first time, that ablation of polyimide by 308-nm XeCl excimer laser radiation generates shock waves at fluences of several times the threshold of ablation. This is a significant finding, because a shock wave, characterized by a picosecond rise time and a supersonic propagation speed, differs qualitatively from an acoustic wave. Our measurements were intended to simulate the ablation of cornea at 193 nm, but are also relevant to material processing of lasers.

We investigated the ablation of sheet polyimide floating on water with a free surface in air, as well as of polyimide immersed in distilled water. The stress waves that are launched in the polyimide during ablation propagate through the 25-μm thick samples and, after a reflection loss, into the water at the rear side of the target. There we determine their propagation speed from a measurement of the time delay between the deflection of two parallel, focused, helium-neon probe beams that are separated by ~40 μm. The velocity measurement suffices to characterize the shock, as the relationship between shock velocity and pressure is

At fluences of only a few times the threshold of ablation F_o the ablation-induced pressure transients propagate at supersonic velocities in the water, indicating the generation of shock waves. The peak pressures of the shocks propagating in the water are measured near the rear surface of the target. Pressure P, increases with fluence F as $(F-F_o)^n$, where $n = 2/3$ if the ablation is in air and $n = 1/2$ if the ablation is confined by water. Figures 1 and 2 show the experimental results.

Also shown in these figures are the theoretical predictions of an ideal gas model that was used earlier by other workers to explain shock generation by confined ablation of metals.[4,5] According to that model the pressure depends only on irradiance and acoustic impedances of the materials involved, provided that the optical absorption coefficient is high enough. It is seen that the model describes the pressures generated by the confined ablation quite successfully.

For ablation in air (Fig. 1) the pressures predicted by the model are lower than the experimental results. This may be due to subsurface heating; if subsurface layers are heated sufficiently rapidly, their expansion can be confined by the overlying material. This implies that even the ablation of a free surface may actually be confined significantly by the target material itself. The confinement effect would increase the ablation pressures. If the energy were deposited deeper in the polyimide sample, possibly by using longer wavelength radiation, the ablation pressures could in principle rise even more. The corresponding model prediction is indicated in Fig. 1 as a dashed line.

Although these measurements were designed to measure the pressures accompanying pulsed excimer ablation, it is worth noting that the same ablation system may now be used as a source of characterized shock waves. Such a source may have use in sonochemistry, as well as in the study of shock effects on cells and macromolecules.

1. P. E. Dyer and R. Srinivasan. Appl. Phys. Lett. 48, 445 (1986).
2. F. W. Cross, R. K. Al-Dhahir, and P. E. Dyer. J. Appl. Phys. 64, 2194 (1988).
3. A. G. Doukas, A. D. Zweig, J. K. Frisoli, R. Birngruber, and T. F. Deutsch. Appl. Phys. B 53, (1991), in press.
4. R. D. Griffin, B. L. Justus, A. J. Campillo, and L. S. Goldberg. J. Appl. Phys. 59, 1968 (1986).
5. R. Fabbro, J. Fournier, P. Ballard, D. Devaux, and J. Virmont. J. Appl. Phys. 68, 775 (1990).

3:30 pm

CThL5 Time resolved transmission of collagen-based films during ArF excimer laser ablation

M. N. Ediger, G. H. Pettit, R. P. Weiblinger, *FDA Center for Devices & Radiological Health, 1901 Chapman Ave., Rockville, MD 20857*

Time resolved reflectivity studies of ArF (193-nm) laser pulses on bovine cornea have shown substantial temporal trunca-

results have also been obtained using collagen gel substrates.[2] These investigations have indicated that this pulse tion is primarily due to dynamic reflectivity changes in the surface, and is not predominantly an effect of scattering by ablation products. Since the underlying physical principles of pulsed, ultraviolet laser tissue ablation are not yet well understood, dynamic changes in the optical properties of the cornea are of interest in the study of the energy deposition and transport. In this work, the time resolved transmission of collagen films and of thin sections of bovine cornea have been measured to provide information about the light/tissue interaction at the surface of collagen-based substrates.

Thin films (<10 μm) of denatured collagen (gelatin) were irradiated with the spatially filtered output of an ArF excimer laser. A typical transmitted waveform occuring at a laser fluence of 110 mJ • cm⁻² is compared with the incident laser pulse in Fig. 1. In this figure, both waveforms have been normalized to equal peak magnitude. Clearly, the transmission of the sample increases over the course of the irradiation pulse. This is in distinct opposition to subablative irradiation where the transmitted waveform exhibits exact correspondence to the pulse shape of the incident laser waveform. Analysis is presented that indicates that the temporal distortion at ablative fluences is not simply due to a reduction in the thickness of the sample by ablation. The actual ablation of the trailing edge of the transmitted pulse correlates with reflectivity measurements in collagen gels.[2] In that work, the reflectivity was observed to fall precipitously in the tail of the pulse, suggesting energy deposition and/or transmission of the sample were radically increasing at the same instant.

The results of transmission experiments performed with thin sections (~10 μm) of bovine cornea are shown in Fig. 2. Again, the incident laser waveform is shown for comparison, and the pulses have been normalized to equal magnitude. The laser fluence for corneal film irradiation was 170 mJ • cm⁻². The transmitted waveform for the corneal film differs considerably in shape from that obtained for gelatin films. Instead, the pulse transmitted by corneal films more resembles the truncated reflected pulse observed from whole, unsectioned corneas. These results suggest that the attenuation of the laser by the intact tissue increases over the course of the ablation pulse.

The dissimilarity in the transmitted pulses of these two collagen-based substrate may be due to the conformational differences in the absorbing protein. These experimental results are presented and contrasted with those obtained using films produced with bovine collagen in its native (nondenatured) conformation.

1. G. H. Pettit, M. N. Ediger, and R. Weiblinger, "Dynamic optical properties of collagen-based tissue during ArF excimer laser ablation", submitted to Appl. Opt., Nov. 1991.
2. M. N. Ediger, G. H. Pettit, and R. Weiblinger, "Bovine corneal photo-

Lecture Notes in Physics

389

J.C. Miller   R.F. Haglund, Jr.   (Eds.)

Laser Ablation

Mechanisms and Applications

Proceedings of a Workshop
Held in Oak Ridge, Tennessee, USA
8–10 April 1991

INFLUENCE OF LIQUEFACTION ON LASER ABLATION: DRILLING DEPTH AND TARGET RECOIL

A.D. Zweig

Wellman Laboratories of Photomedicine
Massachusetts General Hospital
Boston, MA 02114

ABSTRACT

Ablation of materials by highly-absorbed laser pulses (duration 200 μs) is modelled using a steady-state approach that takes into account target liquefaction. Material is removed by a combination of evaporation and ejection of liquid that is caused by radial evaporation-induced pressure gradients at the bottom of the ablation crater. As a result the evaporation rate is reduced and the drilling efficiency enhanced. The model explains experimental drilling-depth and recoil-momentum data.

SUMMARY

Drilling depth and target recoil provide important and easily measurable information on laser ablation. They vary with the distance between the surface of the target and the waist of the laser beam. For laser pulses of several 100 μs duration the observed variation is very similar for biological targets and metals, suggesting that the same physical mechanisms are involved in ablating these materials[1,2].

Targets illuminated with sufficiently intense, highly-absorbed laser radiation are heated at the surface and start to evaporate after a short fraction of the ablating laser pulse. Because of momentum conservation the resulting violent vaporization of material increases the pressure locally. To a first approximation the pressure is proportional to irradiance. The induced pressures vary spatially with the beam profile of the ablating laser. Thus if the target material liquefies prior to evaporation, the pressure-induced shear forces at the surface push material in radial direction towards the crater wall. There the liquid flow changes direction and continues axially, along the wall and out of the hole. This mechanical ejection mechanism becomes more efficient as more liquid moves in the radial direction. Correspondingly, drilling is enhanced by a low viscosity of the molten material, a large thickness of the liquid surface layer, and a small spot size of the drilling beam.

For a given laser pulse the total drilling depth changes with the distance from the surface of the target to the waist of the beam. Under tight focusing conditions the mechanical drilling contribution becomes important, as can be seen from the experimental results presented in Fig. 1a. The solid curve is the result of a model calculation based on a steady-state description of drilling[3]. The calculation took into account the variation of irradiance with distance from the beam waist and used parameters corresponding to the experimental data. Also shown in Fig. 1a is the calculated depth for purely evaporative drilling into a water target (dashed line). As is made clear by the figure,
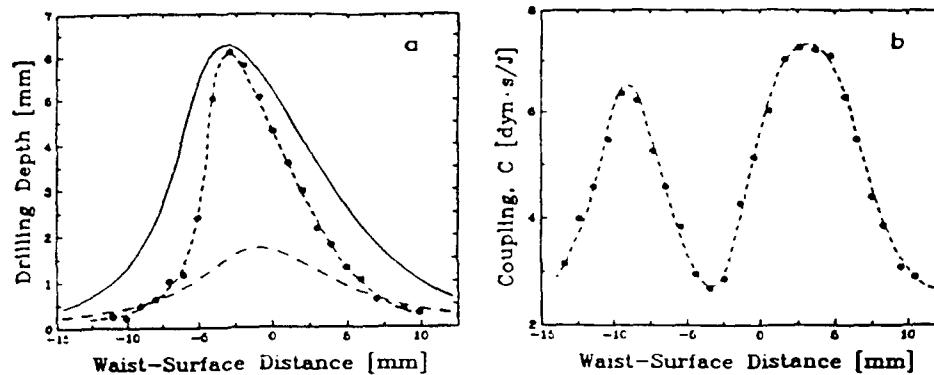
Figure 1: Influence of the initial position of the target surface on the drilling mechanism. Positive (negative) positions correspond to a beam waist located outside (inside) the target. Experimental data for gelatin containing 0.84 g/cm^3 water is indicated by filled circles (•). The short-dashed lines are to guide the eye. All the holes were drilled with single laser pulses ($\lambda = 2.94 \ \mu m$, $\tau = 200 \ \mu s$, $\omega_0 = 72 \ \mu m$, $E_{ir} = 40$ mJ). Data from[1]. (a): Drilling depth versus waist-target distance. The solid line is the result of a model calculation that takes into account evaporation and ejection; the dashed line shows the calculated depth for a purely evaporative drilling. (b): Coupling coefficient, C, versus waist-target distance. C is equal to the total recoil momentum normalized by the laser pulse energy. Note that C has a relative minimum when the drilling depth has a maximum.

the experimental values are too large to be caused by evaporation only. The enhanced drilling depth originates from the ejection mechanism.

The recoil momentum, caused by the ejected material during an ablation process on a target, provides another simple means of characterizing the interaction experimentally. The total recoil momentum divided by the pulse energy is called the mechanical coupling coefficient, C, and has units of dyn · s/J. In Fig. 1b its dependence on the beam waist to target distance is shown. The appearance of that curve is similar for a variety of biological targets as well as metals. It can be explained by the generation of liquid material during ablation.

Neglecting the contribution of liquid ejecta to the total target recoil, the coupling coefficient can be estimated roughly by assuming that all the evaporated material leaves the target at the speed of sound. This picture is valid only if the induced gas flow is one- dimensional. For high aspect-ratio holes this can be expected despite the long pulse durations used (200 μs).

Therefore the recoil curves can be interpreted by considering the influence of aspect-ratio and total mass evaporated as follows: For shallow holes the vapor flows mainly parallel to the target surface, with but a small velocity component perpendicular to the surface of the target. As the radial momentum components cancel each other because